Astronomy & Astrophysics manuscript no. Vanzella
(DOI: will be inserted by hand later)
February 2, 2008

The Great Observatories Origins Deep Survey

VLT/FORS2 Spectroscopy in the GOODS-South Field

E. Vanzella[1,2], S. Cristiani[2], M. Dickinson[3], H. Kuntschner[4], L. A. Moustakas[5], M. Nonino[2], P. Rosati[6], D. Stern[8], C. Cesarsky[6], S. Ettori[6], H. C. Ferguson[5], R.A.E. Fosbury[4], M. Giavalisco[5], J. Haase[4], A. Renzini[6], A. Rettura[6,7], P. Serra[4], and the GOODS Team

[1] Dipartimento di Astronomia dell'Università di Padova, Vicolo dell'Osservatorio 2, I-35122 Padova, Italy.
[2] INAF - Osservatorio Astronomico di Trieste, Via G.B. Tiepolo 11, 40131 Trieste, Italy.
[3] National Optical Astronomy Obs., P.O. Box 26732, Tucson, AZ 85726.
[4] ST-ECF, Karl-Schwarzschild Str. 2, 85748 Garching, Germany.
[5] Space Telescope Science Institute, 3700 San Martin Drive, Baltimore, MD 21218.
[6] European Southern Observatory, Karl-Schwarzschild-Strasse 2, Garching, D-85748, Germany.
[7] Universite' Paris-Sud 11, Rue Georges Clemenceau 15, Orsay, F-91405, France
[8] Jet Propulsion Laboratory, California Institute of Technology, MS 169-506, 4800 Oak Grove Drive, Pasadena, CA 91109 ⋆

Received ; accepted

Abstract. We present the first results of the ESO/GOODS program of spectroscopy of faint galaxies in the Chandra Deep Field South (CDF-S). 399 spectra of 303 unique targets have been obtained in service mode with the FORS2 spectrograph at the ESO/VLT, providing 234 redshift determinations (the median of the redshift distribution is at 1.04). The typical redshift uncertainty is estimated to be $\sigma_z \simeq 0.001$. Galaxies have been color selected in a way that the resulting redshift distribution typically spans from z=0.5 to 2. The reduced spectra and the derived redshifts are released to the community through the ESO web page *http://www.eso.org/science/goods/*. Large scale structure is clearly detected at $z \simeq 0.67, 0.73, 1.10$ and 1.61. Three Lyman-break galaxies have also been included as targets and are confirmed to have redshifts $z = 4.800$, 4.882 and 5.828. In a few cases, we observe clear [OII]3727 rotation curves, even at the relatively low resolution ($\Re = 860$) of the present observations. Assuming that the observed velocity structure is due to dynamically-relaxed rotation, this is an indication of large galactic masses (few times $10^{11} M_\odot$) at $z \sim 1$.

Key words. Cosmology: observations – Cosmology: deep redshift surveys – Cosmology: large scale structure of the universe – Galaxies: evolution.

1. Introduction

The Great Observatories Origins Deep Survey (GOODS) is a public, multifacility project that aims to answer some of the most profound questions in cosmology: how did galaxies form and assemble their stellar mass? When was the morphological differentiation of galaxies established and how did the Hubble Sequence form? How did AGN form and evolve, and what role do they play in galaxy evolution? How much do galaxies and AGN contribute to the extragalactic background light? Is the expansion of the universe dominated by a cosmological constant? A project of this scope requires large and coordinated efforts from many facilities, pushed to their limits, to collect a database of sufficient quality and size for the task at hand. It also requires that the data be readily available to the worldwide community for independent analysis, verification, and follow-up.

The program targets two carefully selected fields, the Hubble Deep Field North (HDF-N) and the Chandra Deep Field South (CDF-S), with three NASA Great Observatories (HST, Spitzer and Chandra), ESA's XMM-Newton, and a wide variety of ground-based facilities. The area common to all the observing programs is 320 arcmin^2, equally divided between the North and South fields. For an overview of GOODS, see Dickinson et al. (2003), Renzini et al. (2002) and Giavalisco et al. (2004a).

Spectroscopy is essential to reach the scientific goals of GOODS. Reliable redshifts provide the time coordinate needed to delineate the evolution of galaxy masses, morphologies, clustering, and star formation. They calibrate the photometric redshifts

Send offprint requests to: E. Vanzella (evanzell@eso.org)

⋆ Based on observations made at the European Southern Observatory, Paranal, Chile (ESO programme 170.A-0788 *The Great Observatories Origins Deep Survey: ESO Public Observations of the SIRTF Legacy/HST Treasury/Chandra Deep Field South.*)

that can be derived from the imaging data at 0.36-8μm. Spectroscopy will measure physical diagnostics for galaxies in the GOODS field (e.g., emission line strengths and ratios to trace star formation, AGN activity, ionization, and chemical abundance; absorption lines and break amplitudes that are related to the stellar population ages). Precise redshifts are also indispensable to properly plan for future follow-up at higher dispersion, e.g., to study galaxy kinematics or detailed spectral-line properties.

The ESO/GOODS spectroscopic program is designed to observe all galaxies for which VLT optical spectroscopy is likely to yield useful data. The program makes full use of the VLT instrument capabilities (FORS2 and VIMOS), matching targets to instrument and disperser combinations in order to maximize the effectiveness of the observations. The magnitude limits and selection bandpasses depend to some degree on the instrumental setup being used. The aim is to reach mag $\sim 24-25$ with adequate S/N, with this limiting magnitude being in the B band for objects observed with the VIMOS LR-Blue grism, in the V band for those observed in the VIMOS LR-Red grism, and in the z band for the objects observed with FORS2. This is not only a practical limit, however, but is also well matched to the scientific aims of the GOODS program. The ACS i_{775} imaging samples rest-frame optical (B-band) light out to $z = 1$, where $i_{775} = 25$ reaches 1.5 to 2 magnitudes past L^*_B. This is also the practical limit for high-quality, quantitative morphological measurements from the ACS images (cf. Abraham et al. 1996). Similarly, $i_{775} = 25$ is ~ 1 mag fainter than the measured L^* UV for $z = 3$ Lyman Break Galaxies (LBGs), and 0.5 mag fainter than that at $z = 4$ (Steidel et al. 1999). These are the limits to which GOODS/SIRTF IRAC data will robustly measure rest-frame near-IR light, and hence constrain the stellar mass.

In this paper we report on the first spectroscopic follow-up campaign in the Chandra Deep Field South (CDF-S), carried out with the FORS2 instrument at the ESO VLT in the period fall 2002 - spring 2003 (the first 9 masks, 348 slits). Further 17 masks have been observed during the period 2003 and early 2004, for which the reduction process has started and will be presented elsewhere (Vanzella et al., in preparation).

The paper is organized as follows: in Sect. 2 we describe the target selection and in Sect. 3 the observations and the reduction. The redshift determination is presented in Sect. 4. In Sect. 5 we discuss the data and in Sect. 6 the conclusions are presented. Throughout this paper the magnitudes are given in the AB system (AB $\equiv 31.4 - 2.5\log\langle f_\nu/\mathrm{nJy}\rangle$), and the ACS F435W, F606W, F775W, and F850LP filters are denoted hereafter as B_{435}, V_{606}, i_{775} and z_{850}, respectively. We assume a cosmology with $\Omega_{\rm tot}, \Omega_M, \Omega_\Lambda = 1.0, 0.3, 0.7$ and $H_0 = 70$ km s^{-1} Mpc^{-1}.

2. Target Selection

Objects were selected as candidates for FORS2 observations primarily based on the expectation that the detection and measurement of their spectral features would benefit from the high throughput and spectral resolution of FORS2, and its reduced fringing at red wavelengths, relative to other instrumental options such as VIMOS. In particular, we expect that the main spectral emission and absorption features for galaxies at $0.8 < z < 1.6$ would appear at very red optical wavelengths, out to $\sim 1\mu$m. Similarly, very faint Lyman break galaxies at $z \gtrsim 4$, selected as B_{435}, V_{606} and i_{775}–dropouts from the GOODS ACS photometry, also benefit greatly from the red throughput and higher spectral resolution of FORS2.

In practice, several categories of object selection criteria were used to ensure a sufficiently high density of target candidates on the sky to efficiently fill out multi-slit masks. Using ACS photometry in the AB magnitude system, these criteria were:

1. Primary catalog: $(i_{775} - z_{850}) > 0.6$ and $z_{850} < 24.5$. This should ensure redshifts $z \gtrsim 0.7$ for ordinary early-type galaxies (whose strongest features are expected to be absorption lines), and higher redshifts for intrinsically bluer galaxies likely to have emission lines.
2. Secondary catalog: $0.45 < (i_{775} - z_{850}) < 0.6$ and $z_{850} < 24.5$.
3. Photometric-redshift sample: $1 < z_{phot} < 2$ and $z_{850} < 24.5$, using an early version of GOODS photometric redshifts like those described by Mobasher et al. 2004.
4. i_{775}-dropout and V_{606}–dropout Lyman break galaxy candidates, selected from the criteria of Dickinson et al. 2004a and Giavalisco et al. 2004b, respectively.
5. A few miscellaneous objects, including host galaxies of supernovae detected in the GOODS ACS observing campaign.

Target selection and mask design for the 2002-3 GOODS/FORS2 campaign was carried out while the GOODS ACS observations were still in progress, and before final ACS data reduction or cataloging could be completed. The targets were therefore selected based on interim data reductions and catalogs, initially based on only one epoch of ACS imaging, and later using the three-epoch ACS stacks and preliminary catalogs described in Giavalisco et al. (2004a). Because of this, the actual magnitudes and colors of the observed galaxies from the final, 5-epoch ACS image stack, which we report here in Table 2, may not exactly match the intent of the original selection criteria. When designing the masks, we generally tried to avoid observing targets that had already been observed in other redshift surveys of this field, namely, the K20 survey of Cimatti et al. (2002) and the survey of X-ray sources by Szokoly et al. 2004.

In the present spectroscopic catalog there are 303 targets, 114 meeting the primary selection criterion and 56 meeting the secondary selection criteria. The other targets belong to the remaining classes.

Table 1. Journal of the MXU Observations.

Mask ID	UT date	exp.time (s)
990247	30Dec.2002 - 2,6Jan. 2003	12×1200
984829	9Dec.2002 - 3,4Jan. 2003	12×1200
985831	5Jan. - 4,7Feb. 2003	15×1200 + 663
973934	7, 30, 31Jan. 2003	12×1200
952426	6,7Jan. 2003	12×1200
981451	31Jan. - 24,27Feb. - 22Nov. - 17Dec. - 30Jul. - 1Aug. 2003	24×1200
995131	5-6 Oct. 2002	8×1800
994852	4 Oct. 2002	8×1800
990652	8Dec. 12Nov. 2002	14×1200 + 300 + 900

3. Observations and Data Reduction

The VLT/FORS2 spectroscopic observations were carried out in service mode during several nights in 2002 and 2003. A summary is presented in Table 1. In all cases the 300I grism was used as dispersing element without order-separating filter. This grism provides a scale of roughly 3.2Å/pixel. The nominal resolution of the configuration was $\mathfrak{R} = \lambda/\Delta\lambda$=860, which corresponds to about 9Å at 8000Å. The spatial scale of FORS2 was 0.126″/pixel, the slit width was always 1″. Dithering of the targets along the slits was applied in order to effectively improve the sky subtraction an the removal of CCD cosmetic defects. The mean shift applied was ±8 pixels.

3.1. Data Reduction

Data were reduced with a semi-automatic pipeline that we have developed on the basis of the MIDAS package (Warmels 1991, using commands of the LONG and MOS contexts (Fig. 1). The frames have been bias-subtracted and flat-fielded. For each slit the sky background was estimated with a second order polynomial fitting. In some cases, better results have been obtained adopting a first order polynomial. The fit has been computed independently in each column inside two windows, above and below the position of the object (if more objects are present in the slit, a suitable modification of the windows is applied).

The resulting dithered, sky-subtracted, two-dimensional frames for each object are then averaged, with the weighting determined based on exposure time, seeing, and meteorlogical conditions. Spatial median filtering has been applied to each dithered exposures to clean the cosmic rays. The FORS2 instrument shows an exquisite response in the red domain (beyond 8000Å), in practice no appreciable residual fringe pattern affects the extracted signal. Rather, the sky residuals dominate the noise in the regions where the intensity and the density of the skylines increase (see Figure 1). The individual dithered sky-subtracted spectra have been visually inspected to verify that the object is indeed in the expected region of the slit. This step is necessary since the applied small spatial offsets between the science exposures can result in objects falling too close to the slit edge or even outside the slit (in exceptional cases). After this visual screening, the *spatial* offset between different exposures of the same object was calculated on the basis of the *world coordinate system* (WCS) information stored in the frame headers. The individual exposures were co-added (including the rejection of bad pixels or cosmic ray hits) after applying these spatial shifts. The frames were shifted in the spatial direction and only by integer numbers of pixels. As the objects were sufficiently well sampled (the pixel scale was significantly smaller than the seeing), no significant blurring of the spectra was observed, while the statistical properties of the individual pixels were preserved.

The position of the target on the detector was estimated by collapsing 700 columns in the dispersion direction and measuring the center of the resulting profile. The 1-D object signal was obtained using the 'optimal extraction' method of MIDAS. This procedure calculates a weighted average in each column, based on both the estimated object profile and photon statistics.

Wavelength calibration was calculated on (daytime) arc calibration frames, using three arc lamps (a He, and two Ar lamps) providing sharp emission lines over the whole spectral range used (6000–10800Å). The object spectra were then rebinned to a linear wavelength scale. We have verified the accuracy of the wavelength calibration by checking the position of 25 narrow skylines in the science exposures (from 5577 to 10400 Å). Systematic translations of the wavelength scale have been typically measured to be of the order of ±1Å and corrected. The final (absolute) mean wavelength accuracy for all spectra is 0.9±0.1Å RMS.

Relative flux calibration was achieved by observations of standard stars listed by Bohlin et al. 1995. Since the standard stars are typically quite blue and second order light can be substantial, the calibration spectra were obtained both with and without order-sorting filters, providing calibration across the entire optical window. As noted previously, we opted to obtain the science target *without* an order-sorting filter, implying deleterious effects to the flux calibration, particularly for bluer objects and at longer wavelengths. For the red objects which dominated the FORS2 target selection, we felt that the improved wavelength coverage

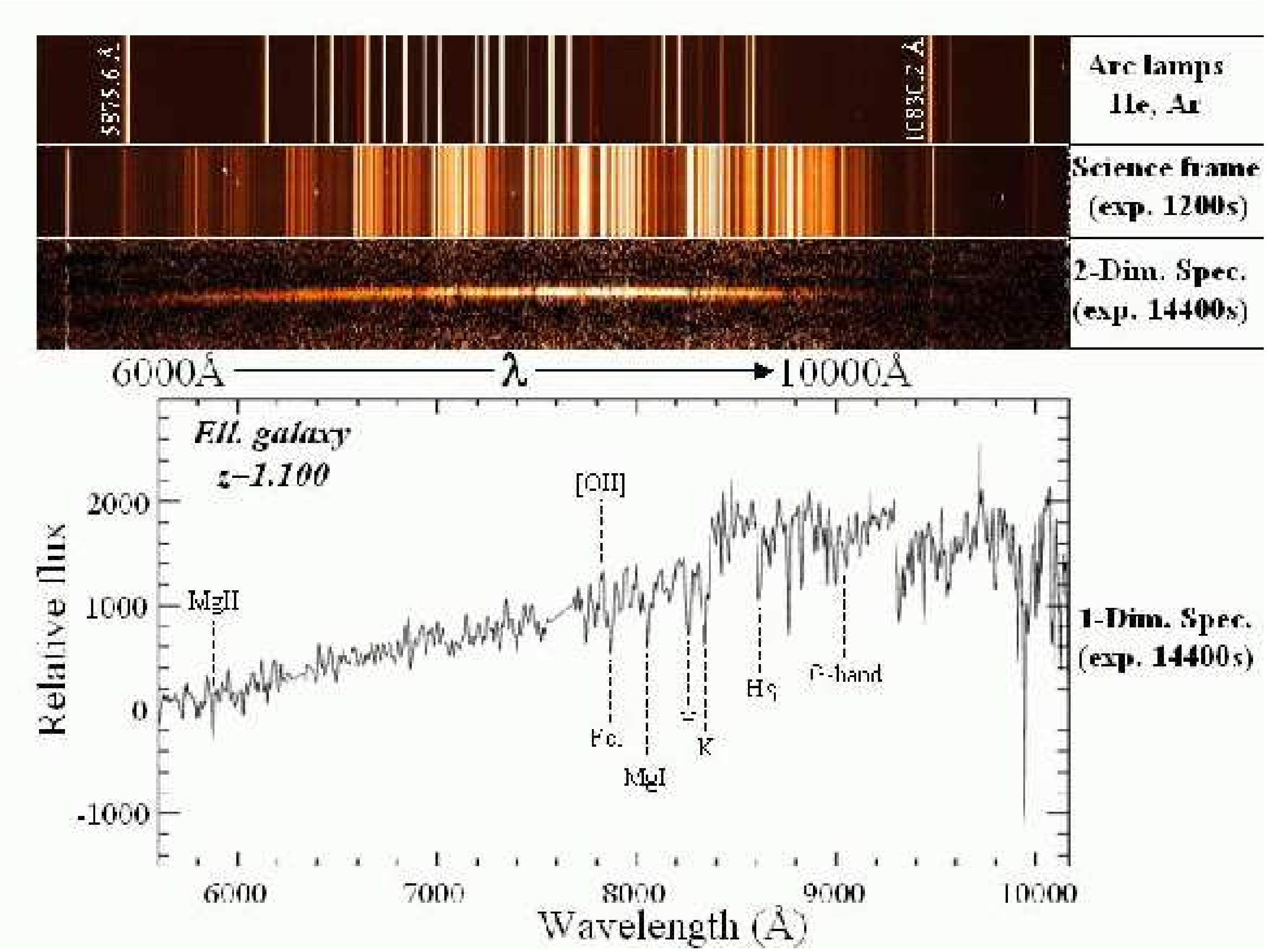

Fig. 1. Typical FORS2 data products for an individual slit of multi-object mask. From the top of the figure: the 2-D spectrum of the arc lines used for the wavelength calibration, a 2-D science exposure (1200 seconds), the final flat-fielded and sky-subtracted 2-D spectrum (co-addition of 12 exposures for a total of 4 h), and at the bottom the 1-D spectrum with the identification of the main absorption and emission lines (in this example an elliptical galaxy at z=1.100, *GDS J*033217.46-275234.8).

more than compensated for the slightly comprimised flux calibration. Due to both this second order light and uncertain slit losses, we caution against using the calibrated fluxes for scientific purposes.

4. Redshift Determination

Spectra of 399 objects have been extracted. From them we have been able to determine 234 redshifts. In the large majority of the cases the redshift has been determined through the identification of prominent features of galaxy spectra: the 4000Å break, Ca H and K, g-band, MgII 2798, AlII 3584 in absorption and Ly_{α}, [O II]3727, [O III]5007, Hβ, Hα in emission. The redshift estimation has been performed cross-correlating the observed spectrum with templates of different spectral types (S0, Sa, Sb, Sc, Ell., Lyman Break, etc.), using the *rvsao* package in the IRAF environment. The redshift identifications are summarized in Table 2 and are available at the URL *http : //www.eso.org/science/goods/*.

In Table 2, the column *ID* contains the target identifier, that is constructed out of the target position (e.g., *GDS J*033206.44-274728.8) where GDS stands for **G**OO**D**S **S**outh. The *quality* flag, indicates the reliability of the redshift determination. Quality "A" indicates a solid redshift determination, "B" a likely redshift determination, "C" a tentative redshift determination and "X" an inconclusive spectrum or three cases in which no extraction was possible. 150 objects have been classified with quality "A", 57 with quality "B", 27 with quality "C", 69 with inconclusive redshift determination "X".

The *class* flag groups the objects for which emission line(s) (em.), absorption-line(s) (abs.) or both (comp.) are detected in the spectrum. The classification has been guided by the observed continuum level and slope blueward and redward of the emission/absorption feature, by the broad-band colors and the morphology of the targets (see Figure 2). 11 objects have been classified as stars.

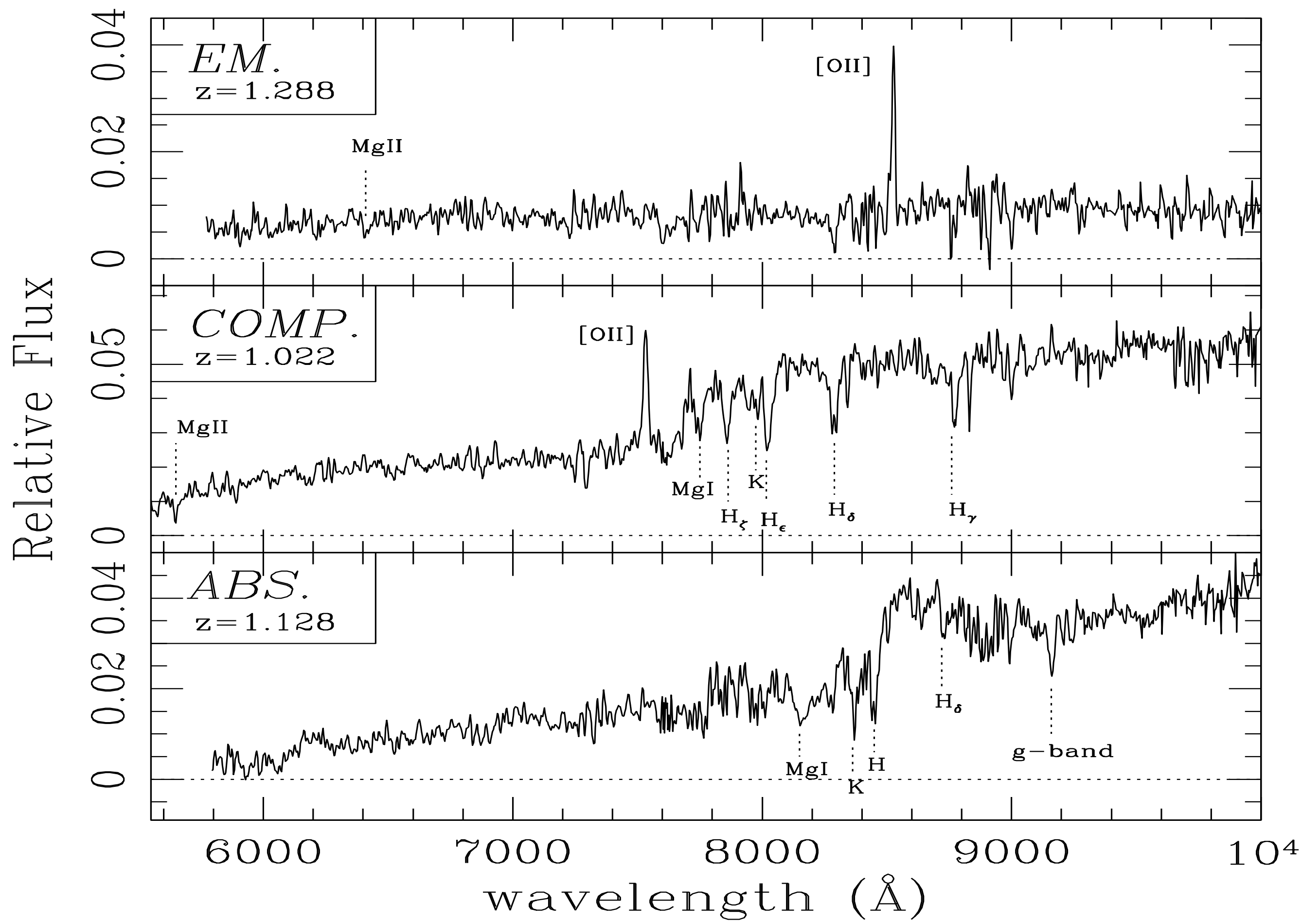

Fig. 2. Three examples of objects classified as "em." (emission-lines detected), "abs." (absorption lines) and "comp." (both emission and absorption lines detected).

In 38% of the cases the redshift is based only on one emission line, usually identified with [O II]3727 or Ly_α. In these cases the continuum shape, the presence of breaks, the absence of other spectral features in the observed spectral range and the broad band photometry are particularly important in the evaluation. In general these solo-emission line redshifts are classified as "likely" (B) or "tentative" (C).

Finally, the *comments* column contains additional information relevant to the particular observation. The most common ones summarize the identification of the principal lines, the inclination of an emission line due to internal kinematics, the weakness of the signal ("faint"), the low S/N of the extracted spectrum ("noisy"), the 20% light radius ("Flux-radius") for objects classified as stars, etc.

There are two objects that are not present in the v1.0 catalog, with $z = 0.957$ and $z = 4.882$ (marked with a cross in the Table 2). These two objects were not successfully deblended in the detection process from the brighter nearby galaxies.

The internal redshift accuracy can be estimated from a sample of 42 galaxies which have been observed twice (or more) in independent FORS2 mask sets. The distribution of measured redshift differences is presented in Figure 4. The mean of the distribution is close to zero (10^{-6}) and the redshift dispersion $\sigma_z = 0.00078$ and mean absolute deviation $< |\Delta z| >= 0.00055$, fairly constant with redshift. These values can be considered as a lower limit to the redshift uncertainty.

5. Discussion

5.1. Reliability of the redshift - comparison with VVDS

A practical way to assess the reliability of the redshifts reported in Table 2 is to compare the present results with independent measurements of other surveys. From this point of view the recent release of the data of the VIMOS-VLT Deep Survey (VVDS, Le Fevre et al. 2004) is particularly important. There are 39 VVDS objects in common with the first release of the FORS2 GOODS survey and Figure 5 shows the comparison of the redshift determinations. The reliability level of the redshift measure-

Table 2. Spectroscopic redshift catalog.

ID(V1)	z_{850}	$(i_{775} - z_{850})$	zspec	class.	Quality	comments
GDS J033206.44-274728.8	21.07	0.70	1.022	comp.	A	[OII], CaHK, MgI
GDS J033210.73-274819.4	24.33	0.96	1.396	em.	C	faint, [OII]
GDS J033210.79-274719.8	25.64	0.06	-	-	X	faint(line@8069A?)
GDS J033210.92-274722.8	19.98	0.29	0.417	em.	B	CaH, g-band, [OIII], Na, Hα
GDS J033210.93-274721.5	22.19	1.00	1.222	abs.	A	CaHK, MgI, Hδ
GDS J033212.00-275104.2	23.00	0.85	1.018	comp.	A	[OII], CaHK, g-band
GDS J033212.47-274621.4	24.06	1.03	-	-	X	faint
GDS J033212.61-274605.1	24.05	0.53	1.378	em.	A	[OII], MgI
GDS J033212.79-274823.1	23.03	0.45	1.316	em.	A	[OII], MgII, (CaHK faint)
GDS J033213.53-274917.0	23.92	0.45	-	-	X	faint
GDS J033214.05-275124.5	22.69	0.74	1.220	em.	A	[OII], MgII
GDS J033214.33-274825.2	24.91	-0.012	-	-	X	featureless continuum
GDS J033214.38-274825.9	27.14	0.24	-	-	X	faint
GDS J033214.69-275258.2	23.82	0.24	1.101	em.	A	[OII]
GDS J033214.71-275257.2	24.27	0.48	1.360	em.	B	[OII]?
GDS J033214.81-274600.0	24.24	0.54	1.370	em.	C	[OII]?
GDS J033214.93-274659.8	23.75	0.12	-	-	X	abs@7080A
GDS J033215.01-274633.4	23.68	0.45	1.000	abs.	C	D4000 break?
GDS J033215.09-275130.7	24.31	0.32	1.229	em.	A	[OII]
GDS J033215.88-274723.1	21.75	0.28	0.896	em.	A	[OII], Hβ, TILT
GDS J033216.02-274750.0	22.83	0.96	1.298	comp.	B	CaHK, [OII](line6255?)
GDS J033216.17-275241.4	22.55	0.78	1.094	abs.	B	CaHK, g-band, MgI-noisy
GDS J033216.28-274955.5	23.72	0.41	-	-	X	featureless continuum
GDS J033216.34-275013.4	23.25	0.52	1.046	comp.	A	[OII](Sky-ABS), CaHK
GDS J033216.37-275201.3	23.28	0.11	-	-	X	bright, abs@6271,6982,7100
GDS J033216.69-275239.0	22.57	0.88	1.045	abs.	A	CaHK, g-band
GDS J033216.91-274808.3	25.37	0.37	-	-	X	faint
GDS J033216.95-274519.3	23.61	0.78	1.303	em.	A	[OII]
GDS J033216.98-275102.4	23.54	0.40	0.991	em.	A	[OII], [OIII], Hβ
GDS J033217.29-274807.5	21.97	0.45	0.735	abs.	A	CaHK
GDS J033217.29-275113.2	22.73	0.85	-	-	X	bad-row, featureless?
GDS J033217.31-275025.0	23.50	0.19	1.612	em.	A	[OII]
GDS J033217.34-274844.3	24.88	0.35	1.107	em.	C	[OII], faint
GDS J033217.46-275234.8	21.93	0.96	1.100	abs.	A	CaHK, MgI
GDS J033217.47-274838.4	22.20	0.18	0.737	em.	A	[OII], [OIII], Hβ
GDS J033217.48-275248.0	21.82	1.08	1.095	abs.	A	CaHK, g-band
GDS J033217.56-274709.2	24.01	0.43	-	-	X	faint
GDS J033217.56-274810.1	24.36	0.13	0.542	em.	C	[OII]?-faint
GDS J033217.62-275228.5	21.18	0.78	1.098	comp.	A	CaHK, MgI, g-band, AlII, [OII]
GDS J033217.63-274811.8	22.57	0.52	0.735	em.	A	[OII], CaHK, [OIII]
GDS J033217.77-274603.0	24.23	0.91	-	-	X	faint
GDS J033217.78-274823.8	22.57	0.08	0.117	em.	B	Hα,[OIII]
GDS J033217.80-275256.9	24.30	0.50	1.044	em.	B	[OII]?(SKY.ABS)
GDS J033217.91-274122.7	22.10	0.96	1.041	abs.	A	CaHK, MgI
GDS J033217.94-274721.5	20.04	0.53	0.732	abs.	A	CaHK, g-band, MgI, Hδ, Hβ, AlII
GDS J033218.01-274718.5	19.41	0.61	0.735	comp.	A	[OII], CaHK(noisy)
GDS J033218.03-274850.3	23.20	0.18	0.297	em.	A	[OIII], Hβ, Hα
GDS J033218.07-274845.7	23.19	0.75	0.000	star	B	star Flux-radius = 1.261
GDS J033218.19-274746.6	23.74	1.49	0.000	star	B	star Flux-radius = 1.256
GDS J033218.24-274744.0	23.63	0.39	-	-	X	featureless continuum
GDS J033218.58-274619.0	23.71	0.56	1.435	em.	A	[OII]
GDS J033218.61-274705.1	23.16	0.41	1.380	em.	A	[OII], MgII
GDS J033218.67-274915.7	24.18	0.28	-	-	X	faint,line@8200A?
GDS J033218.70-274919.8	22.69	0.77	1.038	comp.	A	[OII], CaHK
GDS J033218.78-274951.3	23.82	0.44	1.294	em.	A	[OII], noisy
GDS J033218.79-274820.8	23.41	0.30	0.999	em.	B	[OII]
GDS J033218.81-274908.5	23.90	0.43	1.128	em.	B	[OII]?
GDS J033218.81-274910.0	23.20	0.34	0.735	comp.	A	[OII], CaHK
GDS J033219.15-274040.2	21.11	1.14	1.128	abs.	A	CaHK, MgI, g-band, bright
GDS J033219.23-274545.5	23.44	1.35	0.000	star	C	star? Flux-radius = 1.239
GDS J033219.30-275219.3	22.00	1.14	1.096	abs.	A	CaHK, MgI, g-band

Table 2. Spectroscopic redshift catalog.

ID(V1)	z_{850}	$(i_{775} - z_{850})$	zspec	class.	Quality	comments
GDS J033219.43-274928.2	23.90	0.58	1.048	em.	B	[OII](SKY.ABS)
GDS J033219.48-274216.8	20.29	0.31	0.382	comp.	A	CaHK, low-z
GDS J033219.61-274831.0	21.87	0.10	0.671	em.	A	[OII], [OIII], Hβ
GDS J033219.68-275023.6	20.50	0.25	0.559	comp.	A	[OII], CaHK, [OIII], Hα
GDS J033219.77-274204.0	23.34	0.86	1.044	comp.	A	[OII], CaHK
GDS J033219.79-274609.9	24.11	0.88	1.221	em.	A	[OII], MgI
GDS J033219.79-274839.3	23.55	0.52	1.357	em.	A	[OII]
GDS J033219.89-274517.8	24.00	0.15	-	-	X	bright, abs@8176,6716Å
GDS J033219.96-274449.8	22.35	0.24	0.783	em.	C	[OII]?
GDS J033219.97-274547.6	23.94	0.47	1.219	em.	A	[OII]
GDS J033219.99-274443.2	24.43	0.23	-	-	X	faint
GDS J033220.02-274104.2	21.51	0.52	0.682	abs.	A	CaHK, g-band, MgI
GDS J033220.11-275329.8	24.44	0.75	1.385	em.	C	[OII]?
GDS J033220.28-275233.0	22.22	0.92	1.119	abs.	A	CaHK, MgI, g-band
GDS J033220.29-274718.2	23.94	0.32	-	-	X	faint, noisy
GDS J033220.41-274641.7	24.15	0.35	1.227	em.	A	[OII]
GDS J033220.72-274932.6	24.16	0.80	-	-	X	faint
GDS J033220.91-275344.0	22.99	0.71	1.044	em.	B	[OII](SKY.ABS), CaHK
GDS J033221.22-274625.9	23.48	0.50	1.221	em.	A	[OII]
GDS J033221.57-274941.6	23.01	0.61	1.110	em.	A	[OII]
GDS J033221.63-274800.2	24.35	0.08	-	-	X	featureless continuum
GDS J033221.67-274056.0	22.75	0.65	1.045	em.	B	[OII](SKY.ABS), CaHK
GDS J033221.76-274442.1	20.86	0.18	0.295	em.	A	Hβ, [OIII], Hα
GDS J033221.81-274352.3	24.27	0.58	1.308	em.	B	[OII]
GDS J033221.84-274434.4	24.81	0.36	-	-	X	faint
GDS J033221.99-274655.9	20.42	0.47	0.670	comp.	A	[OII], CaHK, g-band
GDS J033222.18-274659.7	25.00	1.04	-	-	X	faint
GDS J033222.36-275018.4	22.82	0.27	0.736	em.	B	[OII]
GDS J033222.41-274858.0	24.19	0.46	1.383	em.	A	[OII], MgI, MgII
GDS J033222.47-275047.4	24.38	1.79	0.000	star	C	star? Flux-radius = 1.307
GDS J033222.54-274603.8	24.32	0.25	-	-	X	faint(line@9400Å?)
GDS J033222.58-274425.8	20.28	0.33	0.738	comp.	A	[OII], Hβ, CaHK,MgI
GDS J033222.93-274919.1	24.77	0.51	1.298	em.	B	[OII]?
GDS J033222.93-275104.6	22.89	0.38	0.905	em.	A	[OII], Hβ
GDS J033223.17-274219.6	23.82	0.78	-	-	X	faint(abs@8157,9200)
GDS J033223.18-274921.5	24.08	0.55	1.109	em.	B	[OII]
GDS J033223.26-275101.8	21.90	0.85	0.964	abs.	A	CaHK, g-band
GDS J033223.28-274744.7	23.94	0.24	0.764	em.	B	[OII]
GDS J033223.29-274742.6	24.31	0.41	1.092	em.	A	[OII], CaK
GDS J033223.40-274316.6	20.48	0.33	0.615	comp.	A	[OII], CaHK, g-band, Hβ, [OIII]
GDS J033223.45-274709.0	23.22	0.49	1.423	em.	A	[OII], MgII
GDS J033223.61-274601.0	22.57	1.06	1.033	em.	A	[OII], red
GDS J033223.61-275306.3	22.30	0.85	1.125	abs.	C	CaHK? (noisy)
GDS J033223.69-275324.4	20.41	0.40	0.532	comp.	A	[OIII], Hα
GDS J033223.83-274639.4	24.19	0.84	1.222	em.	B	[OII]
GDS J033223.90-275326.2	23.81	1.07	-	-	X	faint
GDS J033224.01-275039.0	22.74	0.98	1.094	abs.	A	CaHK,MgI
GDS J033224.08-275214.6	23.56	0.92	1.015	em.	C	[OII]?, g-band?
GDS J033224.11-274102.1	23.36	0.88	0.000	star	A	star Flux-radius = 1.247
GDS J033224.20-274257.5	24.15	0.32	-	-	X	featureless continuum
GDS J033224.20-274952.9	23.61	0.21	-	-	X	diffuse, faint
GDS J033224.26-274126.4	20.18	0.44	0.533	comp.	A	[OII], [OIII], Hβ, g-band
GDS J033224.37-274315.2	24.63	-0.06	1.271	em.	C	[OII]?
GDS J033224.39-274624.3	21.92	0.76	0.895	abs.	A	CaHK, [OII] faint, (short-slit)
GDS J033224.66-275051.9	22.40	-0.28	0.272	em.	C	Hα, Mg?
GDS J033224.72-274120.4	21.17	0.80	0.967	abs.	A	CaHK, g-band, MgI, AlII
GDS J033224.79-274912.9	24.90	1.61	0.000	star	C	continuum+break, Flux-radius = 1.284
GDS J033224.85-275052.6	23.24	0.61	1.329	em.	A	[OII]
GDS J033224.90-274715.0	24.65	0.71	-	-	X	faint
GDS J033224.91-274923.7	23.87	0.08	-	-	X	featureless bright continuum

Table 2. Spectroscopic redshift catalog.

ID(V1)	z_{850}	$(i_{775}-z_{850})$	zspec	class.	Quality	comments
GDS J033225.04-274718.2	23.86	0.51	1.357	em.	A	[OII], MgII
GDS J033225.10-274219.5	23.65	1.09	1.609	em.	B	[OII]
GDS J033225.19-274735.3	23.90	0.60	1.017	em.	B	[OII], faint
GDS J033225.20-275009.4	22.88	0.95	1.100	abs.	B	CaHK, AlII
GDS J033225.21-275335.0	21.17	0.72	0.833	comp.	A	[OII], [OIII], CaHK, Hδ, (noisy)
GDS J033225.35-274502.8	22.58	0.16	0.975	em.	A	[OII], Hβ, [OIII]
GDS J033225.47-274327.6	20.14	0.51	0.668	abs.	A	CaHK, [OII], AlII
GDS J033225.48-275211.6	23.68	0.39	1.312	em.	B	[OII]
GDS J033225.54-275209.1	22.93	0.45	0.955	em.	B	[OII]?, noisy
GDS J033225.55-275108.2	23.93	0.30	0.832	em.	A	[OII], [OIII], Hβ
GDS J033225.58-274529.0	24.33	0.15	0.667	em.	A	[OII], [OIII]
GDS J033225.69-274347.1	24.73	1.01	-	-	X	faint
GDS J033225.76-274347.0	23.02	1.11	-	-	X	noisy, bad-row
GDS J033225.77-274247.7	24.26	0.62	1.026	em.	B	[OII](SKY.ABS)
GDS J033225.79-274352.3	23.17	0.58	1.297	em.	A	[OII], CaHK
GDS J033225.86-275019.7	21.54	0.48	1.095	em.	A	bright [OII], TILT
GDS J033225.90-274341.2	18.92	0.88	0.000	star	C	star? Flux-radius = 1.296
GDS J033226.00-274150.6	21.75	0.23	0.545	comp.	A	[OII], Hβ, CaHK
GDS J033226.03-275147.7	22.98	0.53	1.242	em.	A	[OII], MgI
GDS J033226.16-274946.5	23.09	0.52	0.735	comp.	A	[OII], CaHK
GDS J033226.17-274603.6	24.25	0.54	1.219	em.	B	[OII]
GDS J033226.24-275005.6	23.68	0.73	1.096	em.	B	[OII]
GDS J033226.26-274209.6	23.96	0.53	0.932	em.	B	[OII]
GDS J033226.31-274722.4	22.48	0.23	0.737	em.	A	[OII], Hβ, [OIII]
GDS J033226.32-274232.3	23.86	0.24	0.736	em.	B	[OII]
GDS J033226.40-274228.2	23.33	0.42	1.615	em.	A	[OII], MgII
GDS J033226.49-274035.5	19.60	0.19	-	-	X	faint
GDS J033226.64-274028.2	21.22	0.21	0.310	em.	A	low-z, Hα, [OIII]
GDS J033226.66-274025.1	21.70	0.29	1.042	em.	C	[OII]?(SKY.ABS)
GDS J033226.66-274029.8	22.06	0.89	1.040	abs.	A	CaHK, g-band, MgI
GDS J033226.67-274758.8	21.81	0.20	0.628	em.	C	Hβ, [OIII]?
GDS J033226.67-274834.8	23.59	0.55	0.905	abs.	C	D4000break?
GDS J033226.84-274545.3	23.47	0.52	1.306	em.	A	[OII]
GDS J033226.89-274541.9	23.72	0.13	0.338	em.	A	[OII], Hβ, [OIII], Hα
GDS J033226.92-274239.8	22.95	0.37	-	-	X	featureless?
GDS J033227.02-274407.2	22.15	0.84	1.128	comp.	A	[OII], CaHK
GDS J033227.05-275318.4	22.25	0.70	1.103	comp.	A	[OII], CaHK
GDS J033227.07-274404.7	22.24	0.16	0.739	em.	A	[OII], Hβ, [OIII]
GDS J033227.11-274922.0	22.88	-0.01	0.559	em.	A	[OII], Hβ, [OIII], Hα
GDS J033227.17-274957.8	23.26	0.51	1.293	em.	A	[OII], CaHK
GDS J033227.36-274204.8	21.26	0.53	0.735	comp.	A	CaHK, MgI, AlII, g-band
GDS J033227.58-274051.7	23.43	0.94	1.070	em.	C	faint, [OII]?
GDS J033227.70-274043.7	21.64	0.86	0.968	abs.	A	CaHK, g-band, AlII
GDS J033227.72-275040.8	21.42	0.74	1.097	comp.	A	[OII], CaHK
GDS J033227.84-274136.8	21.97	0.91	1.043	abs.	A	CaHK, g-band, MgI, AlII
GDS J033227.88-275140.4	20.26	0.40	0.521	abs.	A	CaHK, g-band
GDS J033228.09-275202.4	20.29	0.41	0.560	abs.	A	g-band, Na, Mg, [OIII]
GDS J033228.42-274700.2	24.31	0.19	-	-	X	faint, abs@7060
GDS J033228.44-274703.7	20.86	0.47	-	-	X	noisy
GDS J033228.45-274419.3	22.78	0.50	1.135	em.	A	[OII], MgII
GDS J033228.48-274059.6	23.82	0.49	-	-	X	featureless continuum
GDS J033228.56-274055.7	25.44	0.07	-	-	X	faint
GDS J033228.84-274132.7	25.43	0.01	4.800	em.	C	Ly_{α}? No continuum
GDS J033228.88-274129.3	20.72	0.53	0.733	comp.	A	[OII], CaHK, MgI, g-band, Hδ, Hβ
GDS J033228.94-274600.6	23.82	0.98	-	-	X	abs@8555,8150,9200?
GDS J033228.94-274128.2†	-	-	4.882	em.	B	Ly_{α}, (SiIV?)
GDS J033228.99-274908.4	20.56	0.73	1.095	abs.	A	CaHK, MgI, g-band
GDS J033229.07-274153.1	24.27	0.44	-	-	X	faint
GDS J033229.22-274707.6	20.65	0.51	0.668	abs.	A	CaHK, g-band
GDS J033229.32-274054.0	23.74	0.74	-	-	X	short-slit

† not present in the catalog v1.0

Table 2. Spectroscopic redshift catalog.

ID(V1)	z_{850}	$(i_{775} - z_{850})$	zspec	class.	Quality	comments
GDS J033229.35-275048.5	20.10	0.30	0.415	abs.	A	Hβ, Mg, Na
GDS J033229.48-274036.7	24.04	0.42	1.221	em.	C	[OII]?
GDS J033229.63-274511.3	24.07	0.70	1.033	em.	A	[OII], MgI, CaH
GDS J033229.65-274524.7	24.20	0.73	-	-	X	faint
GDS J033229.71-274507.2	22.24	0.17	0.736	em.	A	[OII], Hβ, [OIII]
GDS J033229.75-275147.1	23.25	0.54	1.315	em.	A	[OII]
GDS J033229.85-274520.5	21.01	0.56	0.953	em.	A	[OII], AlII
GDS J033229.87-274317.7	22.73	0.79	1.097	comp.	B	CaHK, faint [OII]
GDS J033229.99-274322.6	24.42	0.98	-	-	X	faint
GDS J033230.03-275026.8	23.43	0.83	1.005	abs.	B	CaHK, MgII, g-band
GDS J033230.06-274523.5	21.81	0.50	0.955	em.	A	[OII]
GDS J033230.07-274319.0	21.59	0.64	1.101	comp.	B	[OII], CaHK
GDS J033230.09-275100.3	20.80	0.52	0.733	abs.	A	CaHK, g-band, MgI, AlII, Hδ, Hβ
GDS J033230.23-274519.9	23.14	0.09	0.523	em.	A	[OII]
GDS J033230.34-274523.6	21.92	0.07	1.223	comp.	A	faint [OII], CaHK, MgI
GDS J033230.51-275004.4	23.85	1.03	-	-	X	faint
GDS J033230.70-274928.7	22.69	0.16	-	-	X	faint
GDS J033230.71-274617.2	22.24	0.66	1.307	em.	A	[OII], TILT
GDS J033230.75-274306.9	23.25	0.25	0.860	em.	A	[OII], Hβ
GDS J033230.83-274931.8	23.19	0.79	-	-	X	abs@7150,9056? (noisy)
GDS J033230.85-274621.7	21.60	0.74	1.018	comp.	A	CaHK, [OII]
GDS J033230.98-274434.9	23.71	0.50	1.222	em.	A	[OII]
GDS J033231.04-274050.2	21.74	0.77	1.037	abs.	A	CaHK, g-band, MgI
GDS J033231.22-274052.2	22.86	0.58	1.333	em.	B	[OII], noisy
GDS J033231.22-274532.7	22.98	1.00	1.097	abs.	A	CaHK, g-band
GDS J033231.28-274820.2	23.10	0.65	1.173	comp.	A	[OII]
GDS J033231.42-274324.1	23.01	0.82	1.025	em.	B	[OII](SKY.ABS)
GDS J033231.45-274435.0	17.90	0.49	0.000	star	A	star Flux-radius = 1.299
GDS J033231.55-275028.8	23.96	0.68	-	-	X	faint red
GDS J033231.65-274504.8	23.16	0.54	1.098	em.	A	[OII], MgI, CaHK, Hδ, Hγ
GDS J033232.04-274451.7	21.59	0.68	0.895	abs.	A	CaHK
GDS J033232.08-274119.4	22.59	0.53	1.036	em.	B	[OII](SKY.ABS)
GDS J033232.08-274155.2	23.00	0.39	0.960	abs.	C	abs@7000,6400,7800
GDS J033232.12-274359.3	24.66	0.18	-	-	X	faint (line at 6217A?)
GDS J033232.14-274349.9	23.12	0.36	0.973	em.	A	[OII]
GDS J033232.32-274343.6	22.80	0.07	0.533	em.	C	[OIII]
GDS J033232.33-274345.8	23.95	0.42	1.025	em.	B	[OII]
GDS J033232.58-275053.9	21.61	0.21	0.669	em.	B	[OII], Hβ
GDS J033232.73-274538.8	21.69	0.31	-	-	X	short-slit(line5900A)
GDS J033232.73-275102.5	20.78	0.58	0.735	abs.	A	CaHK, g-band
GDS J033232.94-274543.9†	-	-	0.957	em.	A	[OII]
GDS J033232.96-274545.7	19.84	0.33	0.366	abs.	A	N[II]+abs.spec.
GDS J033233.00-275030.2	20.85	0.44	0.669	em.	A	[OII], [OIII], Hβ
GDS J033233.01-274829.4	22.80	0.12	0.664	em.	A	[OIII], Hβ
GDS J033233.02-274547.4	21.13	0.63	0.953	abs.	B	CaHK, [OII]
GDS J033233.08-275123.9	21.39	0.47	0.735	abs.	A	CaHK
GDS J033233.25-274117.4	24.06	0.86	-	-	X	continuum, faint
GDS J033233.28-274236.0	24.55	1.09	1.215	em.	B	[OII], faint red (XCDFS265)
GDS J033233.41-274230.5	23.37	0.06	0.975	em.	B	[OII]
GDS J033233.71-274210.2	23.71	0.46	1.043	em.	B	[OII](SKY.ABS), TILT
GDS J033233.82-274410.0	21.11	0.42	0.667	abs.	A	CaHK, g-band
GDS J033233.85-274600.2	23.82	1.05	1.910	abs.	B	MgII
GDS J033234.00-274412.1	23.70	0.53	0.896	em.	B	[OII], CaHK?
GDS J033234.05-274937.8	22.91	0.71	0.832	comp.	A	[OII], CaHK
GDS J033234.08-274222.3	23.91	0.72	1.476	em.	B	[OII]
GDS J033234.82-274835.5	22.94	0.66	1.245	em.	A	[OII], CaHK
GDS J033234.85-274640.4	22.70	0.61	1.099	em.	A	[OII]
GDS J033235.08-274615.7	23.11	0.63	1.316	em.	A	[OII]
GDS J033235.11-275009.0	24.17	0.44	1.295	em.	A	[OII]

† not present in the catalog v1.0

Table 2. Spectroscopic redshift catalog.

ID(V1)	z_{850}	$(i_{775} - z_{850})$	zspec	class.	Quality	comments
GDS J033235.19-275103.4	24.41	0.23	0.981	em.	B	[OII]?
GDS J033235.26-275104.8	22.79	0.44	0.734	abs.	A	CaHK, Hδ, MgI
GDS J033235.78-274627.5	22.76	0.89	1.094	comp.	A	[OII], CaHK
GDS J033235.79-274734.7	23.65	0.88	1.223	em.	A	[OII], [NeIII]
GDS J033236.04-275004.3	23.40	0.81	1.612	em.	A	[OII], MgII
GDS J033236.39-274747.0	23.18	0.17	-	-	X	abs@6500,6586
GDS J033236.43-274750.6	22.41	0.13	0.127	em.	B	Hα, [OI]6300Å, Na
GDS J033237.19-274608.1	20.90	1.07	1.096	abs.	A	CaHK
GDS J033237.26-274610.3	22.17	0.19	0.736	comp.	A	[OII], CaHK
GDS J033237.56-274646.7	24.89	0.78	-	-	X	abs@8195, em@8949?
GDS J033238.27-274604.0	24.46	1.07	-	-	X	faint
GDS J033238.49-274702.4	21.26	0.76	0.953	abs.	A	CaHK, MgI
GDS J033239.01-274722.7	24.40	0.40	-	-	X	faint
GDS J033239.35-275016.3	22.05	0.42	-	-	X	smoothly-red
GDS J033239.56-274851.7	22.55	0.81	0.000	star	C	star Flux-radius = 1.269
GDS J033239.60-274909.6	20.72	0.89	0.980	abs.	A	CaHK, g-band, AlII
GDS J033239.64-274709.1	22.70	0.99	1.317	comp.	A	[OII], CaHK, MgI
GDS J033239.67-274850.6	24.55	0.21	-	-	X	featureless continuum
GDS J033239.99-275114.2	23.75	0.62	-	-	X	lines:8210,8800?
GDS J033240.01-274815.0	25.33	1.44	5.828	em.	A	Ly_{α}
GDS J033240.67-275032.3	24.56	0.21	-	-	X	bad-row, faint
GDS J033240.79-275035.1	21.69	0.12	0.213	em.	A	Hα, S[II], (2d-order-light)
GDS J033240.92-274823.8	24.00	0.45	1.244	em.	B	[OII]?
GDS J033241.21-274932.4	24.26	0.94	-	-	X	faint
GDS J033241.41-274457.5	23.02	0.80	-	em.	X	em.lines@6815,8208
GDS J033241.48-274440.4	23.00	0.84	1.296	em.	B	[OII], faint
GDS J033241.59-275003.0	22.32	0.66	0.000	star	B	compact, Flux-radius = 1.279
GDS J033241.67-274448.7	23.83	0.14	-	-	X	faint, short-slit
GDS J033241.76-274619.4	20.93	0.35	0.333	em.	C	low-z, Hα
GDS J033242.07-274911.6	23.42	1.30	0.000	star	B	star Flux-radius = 1.253
GDS J033242.21-274953.9	23.83	0.37	1.377	em.	A	[OII], MgI
GDS J033242.25-274625.4	22.50	0.63	1.288	em.	A	[OII], MgII
GDS J033242.32-274950.3	20.33	0.29	-	-	X	noisy
GDS J033242.38-274707.6	23.18	1.11	1.314	abs.	B	[OII], CaHK
GDS J033242.56-274550.2	22.21	0.16	0.218	em.	A	[OIII], Hβ, Hα
GDS J033242.97-274649.9	23.44	0.89	-	-	X	faint
GDS J033244.18-274729.4	23.55	0.44	1.220	em.	A	[OII]
GDS J033244.20-274733.5	21.53	0.20	0.737	em.	A	[OII], [OIII], Hβ
GDS J033244.23-275039.5	24.72	0.40	1.122	em.	B	[OII]?
GDS J033244.29-275009.7	22.62	0.86	1.038	abs.	A	CaHK, g-band
GDS J033244.43-274641.8	22.55	0.13	0.215	em.	C	Hα?
GDS J033244.62-274632.2	23.20	0.44	1.426	em.	A	[OII], MgII
GDS J033244.80-274920.6	23.69	0.84	-	-	X	faint
GDS J033245.15-274940.0	21.92	1.04	1.123	abs.	A	CaHK, g-band, MgI
GDS J033245.21-274858.0	24.65	0.51	1.463	em.	A	[OII]
GDS J033245.90-274517.2	23.79	0.39	1.036	em.	A	[OII], CaHK
GDS J033247.45-274603.9	23.98	0.51	-	-	X	faint
GDS J033248.56-274504.6	22.19	0.88	1.115	abs.	C	CaHK, noisy
GDS J033249.04-275015.5	22.36	0.80	1.122	em.	B	[OII]
GDS J033249.09-274519.2	21.46	0.37	-	-	X	featureless continuum
GDS J033249.11-274524.2	21.81	0.60	1.094	em.	A	[OII], Hβ-faint
GDS J033249.49-274534.2	23.94	0.17	1.609	em.	A	[OII]
GDS J033249.85-274757.8	22.78	0.67	1.146	em.	B	[OII]?
GDS J033250.69-274732.2	23.51	-0.02	-	-	X	em@7100A, abs8100A
GDS J033251.34-274742.7	24.09	0.76	1.298	em.	B	[OII], noisy
GDS J033251.57-275044.7	22.48	0.52	0.980	comp.	A	[OII], Hβ
GDS J033252.87-275114.7	21.20	0.63	1.002	comp.	A	CaHK, [OII]
GDS J033252.88-275119.8	21.84	0.47	1.220	em.	A	[OII], CaHK
GDS J033253.01-275000.5	24.05	0.09	-	-	X	faint
GDS J033253.34-275104.6	25.50	-0.08	0.912	em.	C	noisy, [OII]?
GDS J033255.00-275051.6	21.70	0.37	-	-	X	featureless continuum

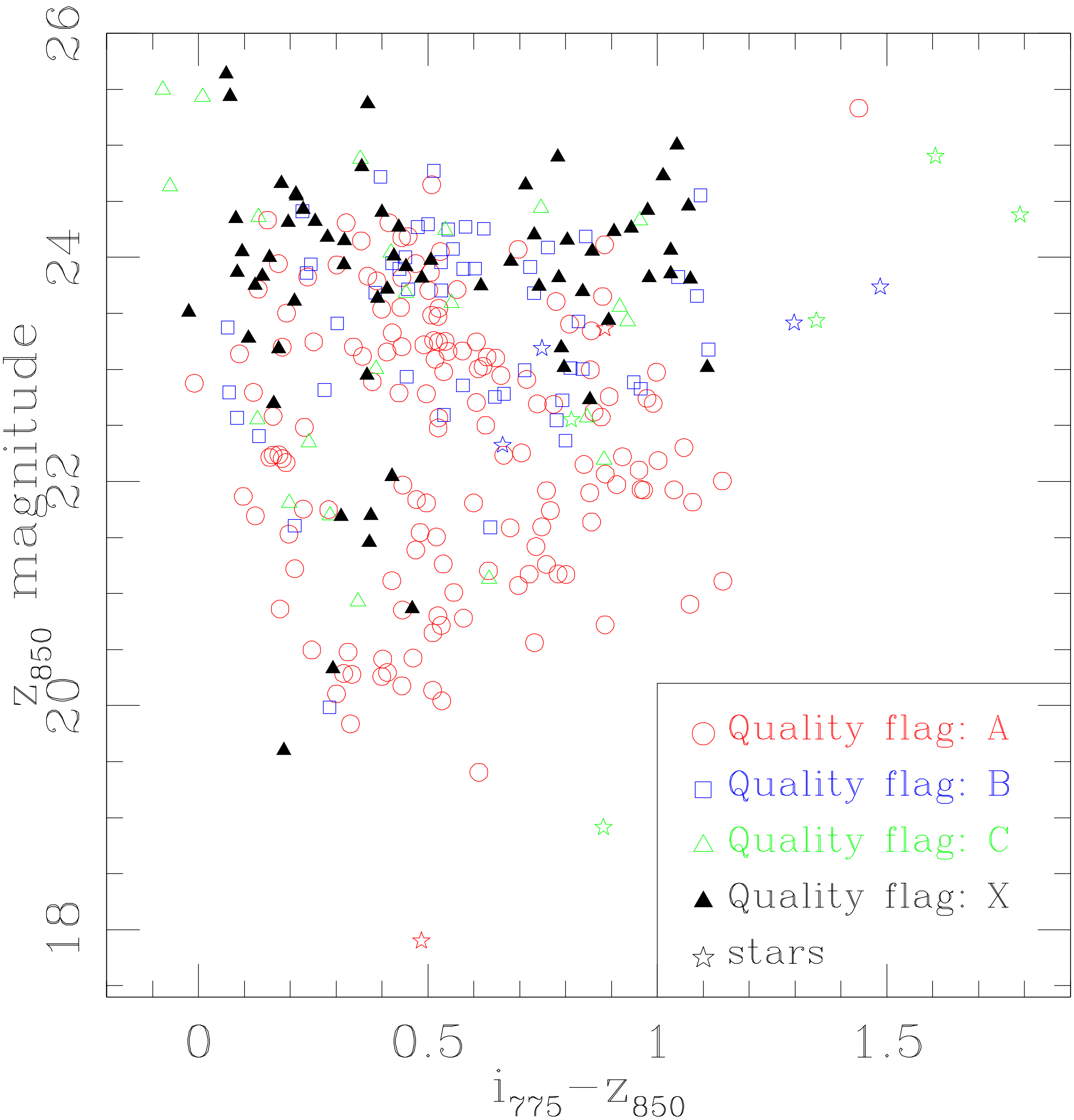

Fig. 3. Color-magnitude diagram for the spectroscopic sample as a function of the quality flag. The uncertainties in the redshift determination increase with increasing z_{850} magnitude. Few bright sources (often serendipitous; $z_{850} < 22$) have inconclusive redshift determinations due to the dithering procedure, which has positioned these sources off the slitlets for many of the exposures.

ments in the VVDS is indicated by a quality flag. Flags 2, 3, 4 are the most secure with a confidence of 75%, 95% and 100% respectively. Flag 1 is an indicative measurement, flag 9 indicates that there is only one secure emission line, and flag 0 indicates a measurement failure with no features identified.

For 29 cases out of 39 (74%) the agreement is very good, with a mean difference $< z_{FORS2} - z_{VVDS} > = 0.0016 \pm 0.0021$.

Assuming equipartition of the redshift uncertainties between FORS2 and VVDS, we can estimate a $\sigma_z(FORS2) \simeq 0.0015$, in reasonable agreement with the estimate of Sect. 4. In the following we will assume a typical uncertainty of the redshift determinations of the present survey to be $\sigma_z \simeq 0.001$ (excluding "catastrophic" discrepancies).

Ten cases show "catastrophic" discrepancies, i.e. $< z_{FORS2} - z_{VVDS} >$ greater than 0.015 and are reported in Table 3.

In the following we discuss case by case the origin of the discrepancy:

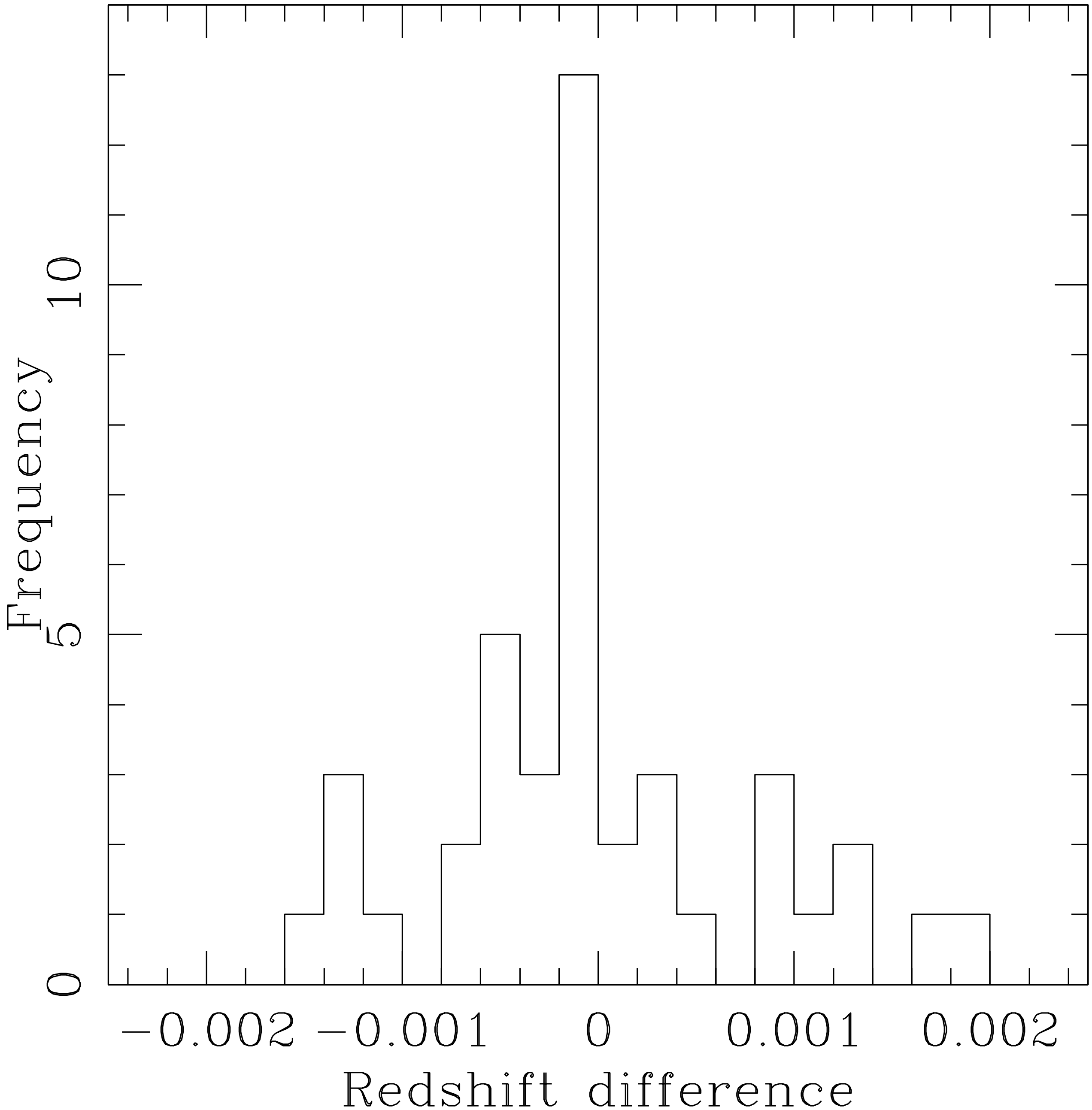

Fig. 4. Redshift differences between objects observed twice or more in independent FORS2 observations. The distribution has a dispersion $\sigma_z = 0.00078$.

1. GDS J033214.05-275124.5:
   - FORS2: the emission line [O II]3727 and the absorption lines Ca H and K are detected in the FORS2 spectrum at z=1.220. The absorption line MgII 2798 is also present at 6210Å. The 4000Å Balmer Break is also evident, quality flag "A".
   - VVDS: the main emission feature in the VIMOS spectrum is identified with [O II]3727 at z=1.325, quality flag 3. We note an absorption feature in the VIMOS spectrum (without identification) at ~6200Å, consistent with the one measured in the FORS2 spectrum.
2. GDS J033219.79-274839.3:
   - FORS2: flat continuum with an evident emission line at ~8784Å. We interpret it as [O II]3727. No spectroscopic feature is observed at ~ 6500Å. Quality flag A.
   - VVDS: the main feature in the VIMOS spectrum is identified with [O III]5007 at z=0.568 (emission line at 7851Å), quality flag 2.

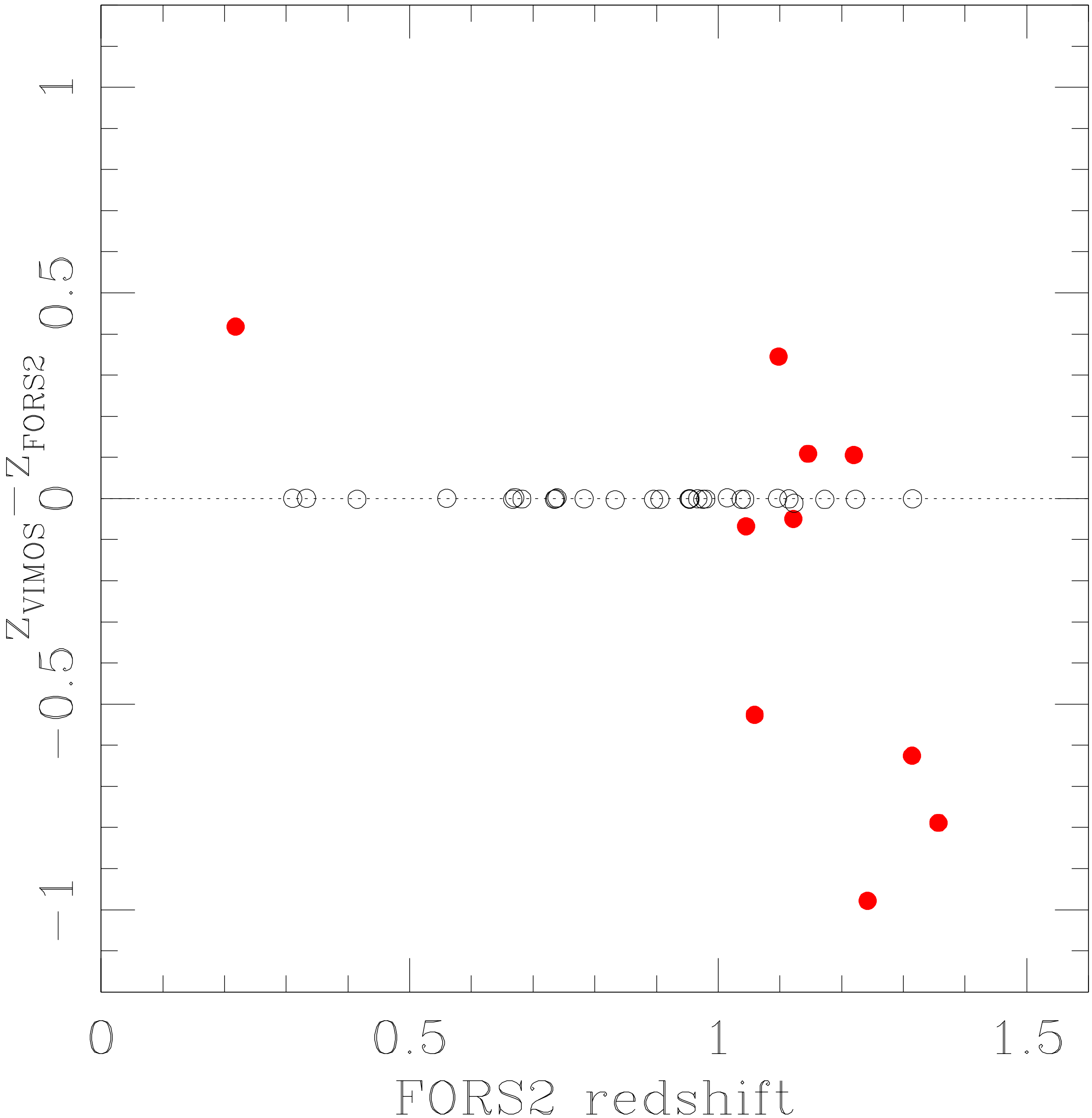

Fig. 5. VVDS spectroscopic redshift versus FORS2 spectroscopic redshift. There are 39 galaxies in common between the VVDS sample and the sample presented in this work. 10 cases show (filled symbols) discrepant redshift determination with $|dz| > 0.015$.

3. GDS J033221.67-274056.0:
   – FORS2: the emission line [O ii]3727 and the absorption lines Ca H and K are detected in the FORS2 spectrum at $z = 1.045$, quality flag “B”. The [O ii]3727 line is attenuated by the sky absorption band at ∼7600Å.
   – VVDS: Ca H and K are identified in the VIMOS spectrum at z=0.977, quality flag 1.
4. GDS J033226.03-275147.7:
   – FORS2: the emission line [O ii]3727 (at 8356Å) and the absorption lines Ca H and K, MgI and B2630 are detected in the FORS2 spectrum at $z = 1.242$, quality flag “A”.
   – VVDS: the main feature is identified with Hα at z=0.264 (at 8296Å), quality flag 9. No emission lines are present in the FORS2 spectrum at this wavelength.
5. GDS J033231.65-274504.8:

Table 3. Galaxies with discrepant redshifts between the FORS2 and VVDS surveys.

N	ID	z(FORS2)	QF(FORS2)	z(VVDS)	QF(VVDS)	z(FORS2)-z(VVDS)
1	GDS J033214.05-275124.5	1.220	A (em.)	1.325	3	-0.105
2	GDS J033219.79-274839.3	1.357	A (em.)	0.568	2	0.789
3	GDS J033221.67-274056.0	1.045	B (em.)	0.978	1	0.067
4	GDS J033226.03-275147.7	1.242	A (em.)	0.264	9	0.978
5	GDS J033231.65-274504.8	1.098	A (em.)	1.443	1	-0.350
6	GDS J033232.32-274343.6	1.059†	C (em.)	0.533	3	0.526
7	GDS J033242.38-274707.6	1.314	B (abs.)	0.688	2	0.626
8	GDS J033242.56-274550.2	0.218	A (em.)	0.635	2	-0.417
9	GDS J033249.04-275015.5	1.122	B (em.)	1.072	2	0.05
10	GDS J033249.85-274757.8	1.146	B (em.)	1.254	2	-0.105

† Adopted FORS2 value has been updated to VVDS value in Table 2.

- FORS2: the emission line [O II]3727 and the absorption lines Ca H and K, MgI, Hδ and are detected in the FORS2 spectrum at $z = 1.098$; the emission line Hγ is also detected at ~9105Å, quality flag "A".
- VVDS: in the VIMOS spectrum a line is detected at ~9105Å, interpreted as [O II]3727 at z=1.443, quality flag 1.

6. GDS J033232.32-274343.6:
   - FORS2: for this object (at the border of the FORS2 field of view) the spectrum starts at ~6400Å. We detect a weak emission line at ~7654Å (close to a sky absorption band), that we originally interpreted to be [O II]3727 at z~1.059, assigning to the redshift a quality flag "C".
   - VVDS: in the VIMOS spectrum an emission line at ~5713Å is detected, interpreted as [O II]3727 at z=0.533 and quality flag 3 (the absorption feature Ca H at ~6085Å is also present). It is consistent with the interpretation [O II]3727 at $z = 0.533$ with the FORS2 ~ 7654Å emission line identified as [O III]5007 at $z = 0.533$. We have therefore updated the entry in Table 2 to a redshift $z = 0.533$.
7. GDS J033242.38-274707.6:
   - FORS2: this is a red object ($i_{775} - z_{850} = 1.11$), we detect two clear absorption features in the ~ 9100Å sky free region interpreted as Ca H and K, faint [O II]3727 seems to be present, quality flag "B".
   - VVDS: red spectrum, Ca H and K are identified in the VIMOS spectrum at z=0.688, quality flag 2.
8. GDS J033242.56-274550.2:
   - FORS2: the emission lines [O III]5007 (at 6098Å), Hβ (at 5921 Å) and Hα (at 7994Å) are detected in the FORS2 spectrum, z=0.218, quality flag "A".
   - VVDS: the main emission feature (at 6094Å) is identified with [O II]3727 at z=0.635, quality flag 2.
9. GDS J033249.04-275015.5:
   - FORS2: the spectrum starts at ~6400Å. It shows continuum with a evident emission line at ~7909Å interpreted as [O II]3727 (z=1.122), a discontinuity consistent with the 4000Å Balmer Break is present, quality flag "B".
   - VVDS: the main feature in the VIMOS spectrum is an emission line at 7723Åidentified with [O II]3727 at z=1.072, quality flag 2.
10. GDS J033249.85-274757.8:
    - FORS2: object red with bright continuum, the emission line [O II]3727 and the absorption lines MgII 2798 and $H\zeta$ are detected in the FORS2 spectrum, the 4000Å Balmer Break is also evident, quality flag "B".
    - VVDS: flat continuum, the NeV absorption line is identified at z=1.254, quality flag 2.

In summary, out of ten highly discrepant cases we have found only one that can be ascribed to an evident error in the identification of the features in the FORS2 spectrum (and the original quality flag for this object was "C"). We conclude that the probable fraction of "catastrophic" misidentifications in Table 2 is at most a few percent.

5.2. Reliability of the redshifts - diagnostic diagrams

As mentioned above, the photometric information and its relation with the redshift provides useful indications about possible errors in the redshift measurement and/or magnitude estimation. The Figures 6, 7 and 8 show the redshift-magnitude, the color-redshift and the color-magnitude distributions for the spectroscopic sample (the quality flag "A" and "B" have been selected in the Figures 7 and 8, while all sources have been plotted in the Figure 6). In figure 7 the two populations of "emission-line" and "absorption-line" (typically elliptical) galaxies are clearly separated. The mean color of the "absorption-line" objects increases from $i_{775} - z_{850} = 0.46 \pm 0.079$ at $< z > = 0.6$ to $i_{775} - z_{850} = 0.86 \pm 0.18$ at $< z > = 1.0$, consistent but increasingly bluer than the colors of a non-evolving $L^\star$ elliptical galaxy (estimated integrating the spectral templates of Coleman, Wu & Weedman (1980) through the ACS bandpasses).

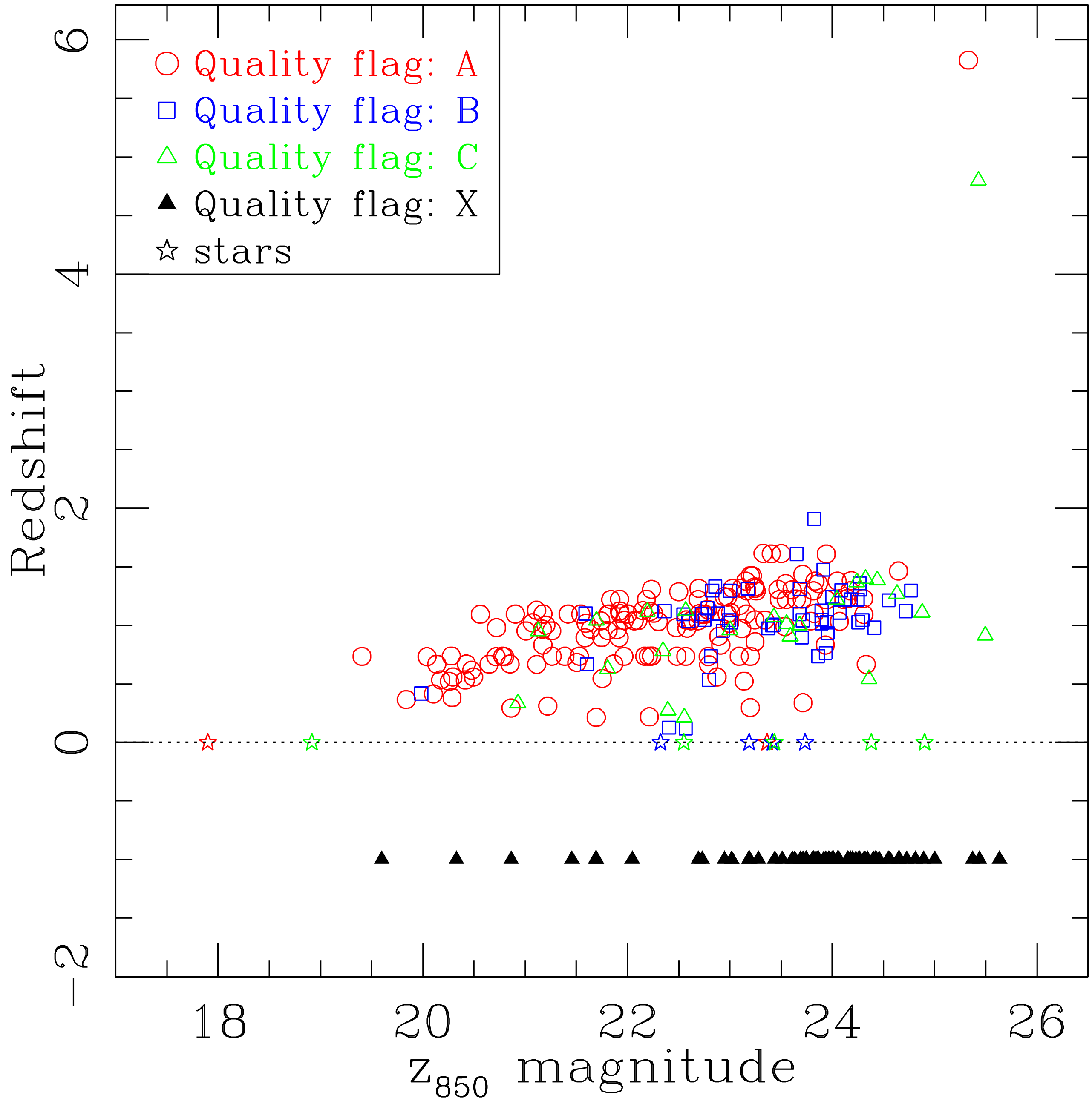

Fig. 6. Spectroscopic redshift versus magnitude for the entire FORS2 sample (quality flag "A", "B", "C" and "X"). Stars are denoted by star-like symbols at zero redshift. Inconclusive spectra are placed at $z = -1$.

The "emission-line" objects show in general a bluer $i_{775} - z_{850}$ color and a broader distribution than the "absorption-line" sources: $i_{775} - z_{850} = 0.16 \pm 0.13$ at $< z > = 0.6$ and $i_{775} - z_{850} = 0.52 \pm 0.21$ at $< z > = 1.1$. The broader distribution, with some of the "emission-line" objects entering the color regime of the ellipticals, is possibly explained by dust obscuration, high metallicity or strong line emission in the z_{850} band.

5.3. Redshift distribution and Large Scale Structure

Figure 9 shows the redshift distribution of the objects observed in the present survey. The majority of the sources are at redshift around ~1 (the median of the redshift distribution is at 1.04), in agreement with the main criterion for the target selection (see Sect. 2). Table 4 shows the fraction of determined redshifts as a function of the spectral features identified, i.e. emission lines, absorption lines, emission & absorption lines, and no reliable spectral features (unclassified). There are 49 galaxies identified

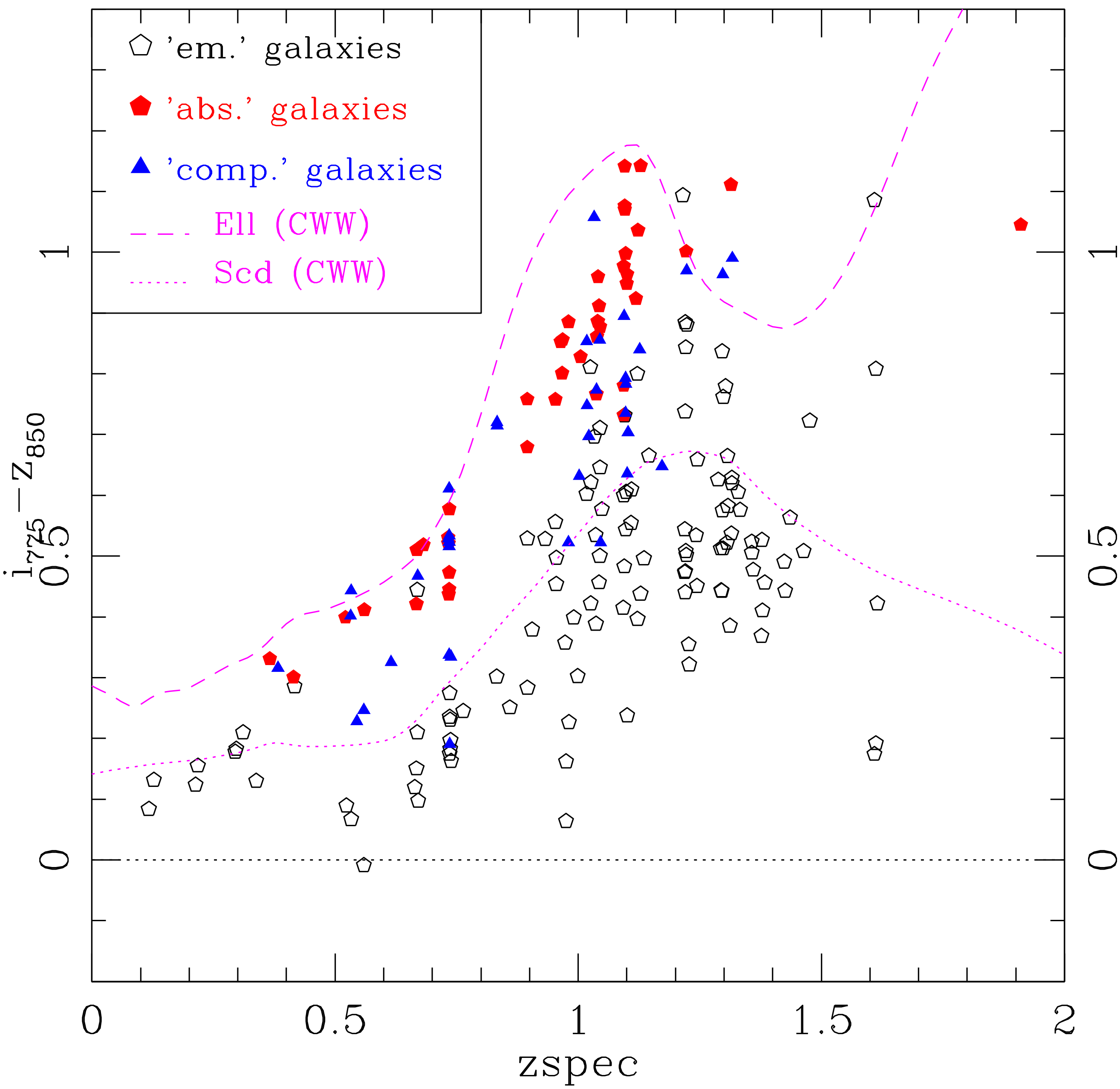

Fig. 7. Color-redshift diagram of the spectroscopic sample. Only redshifts with quality flag "A" and "B" have been selected. Filled pentagons symbols are objects identified with absorption features only ("abs." sources), while open pentagons are objects showing only emission lines ("em." sources). The intermediate cases are shown by filled triangles ("comp." sources). The long-dashed line and the short dashed line show the colors of a non-evolving $L^{\star}$ elliptical galaxy and an Scd galaxy, respectively, estimated integrating the spectral templates of Coleman, Wu & Weedman (1980) through the ACS bandpasses.

with absorption lines only (mainly Ca H and K) in the range of redshift between 0.4-1.3; an example is shown in Figure 1. In 46% of the total sample we have measured emission lines (mainly [O II]3727), many of them entering the so-called "spectroscopic desert" up to z=1.61.

The main peaks in the redshift distribution are at $z \sim 0.73$ (21 galaxies) and 1.1 (25 galaxies). Two concentrations at $z \sim 1.6$ (with 5 galaxies at the mean redshift $< z >= 1.612 \pm 0.003$, see the two dimensional spectra in Figure 11) and $z \sim 0.67$ (9 galaxies) are also apparent. The presence in the CDF-S of large scale structure, (LSS) at $z \sim 0.73$ and $z \sim 0.67$ is already known (Cimatti et al. (2002), Gilli et al. 2003, Le Fevre et al. 2004). The peak at $z \sim 1.1$ seems to be a new indication of large scale

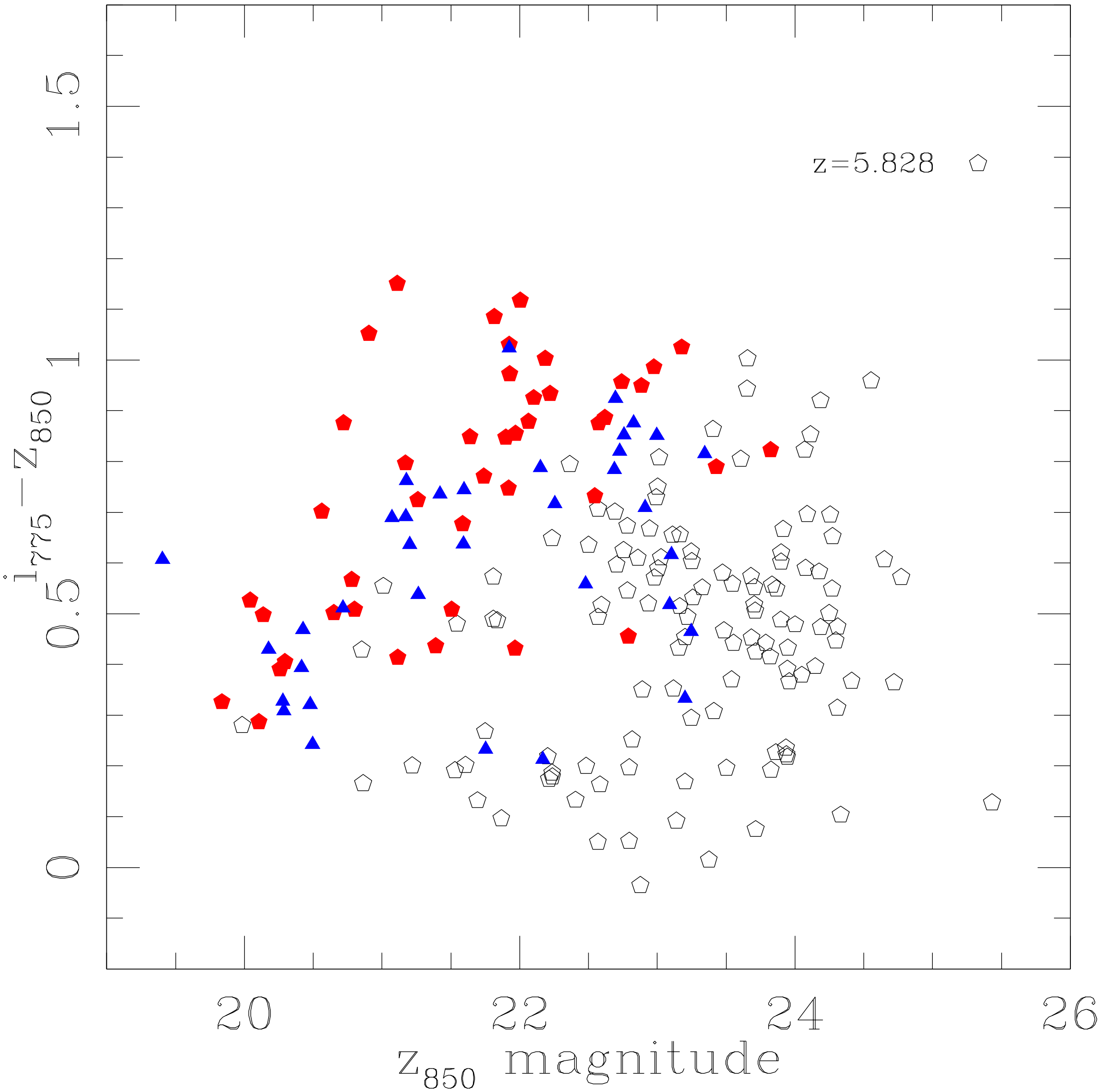

Fig. 8. Color-magnitude diagram for the spectroscopic sample. Only redshifts with quality flag "A" and "B" have been selected. The symbols are the same as in Figure 7.

structure, of the 25 galaxies in the range 1.09<z<1.11, 10 show emission lines, 9 are ellipticals and 6 are intermediate-type galaxies.

The significance of the LSS at z = 1.61 is confirmed by:

1. the observations of Gilli et al. (2003) who found a peak in the redshift distribution of X-ray sources at z=1.618 (5 galaxies) and measured a Poissonian probability of 3.8×10^{-3} for a chance distribution ;
2. three more galaxies at z = 1.605, 1.610, 1.615 in the K20 survey Cimatti et al. (2002);

The structure at $z \approx 1.61$ is extending across a transverse size of ~ 5 Mpc in a wall-like pattern rather than a group structure (see Fig. 10).

Table 4. Fractions of sources with different spectral features.

Spectral class	z_{mean}	z_{min}	z_{max}	Fraction
emission	1.131	0.117	5.828	46%
absorption	0.950	0.366	1.910	16%
em. & abs.	0.897	0.382	1.317	12%
stars	0.000	0.000	0.000	4%
unclassified	-	-	-	22%

5.4. High redshift galaxies

As discussed in Sect. 2, the target selection includes mainly low redshift objects ($z < 2$). For three galaxies, however, a redshift larger than four was measured: the galaxy $GDS\ J033240.01-274815.0$ at $z = 5.828$ the only i_{775}-dropout (see Sect. 2) actually targeted in the present observations and two serendipitously-observed high redshift sources, $GDS\ J033228.84-274132.7$ and one object at $\alpha = 3^h\ 32^m\ 28.94^s$, $\delta = -27^\circ\ 41'\ 28.19''$ not present in the catalog v1.0, measured at $z = 4.800$ and $z = 4.882$, respectively.

The *i*-dropout candidate has been observed with both the Keck and VLT telescopes (Dickinson et al. 2004a). In Figure 12 the FORS2 spectrum of the *i*-dropout source is shown. The Ly_α line is clearly detected at $z = 5.828$ and shows the blue cut–off characteristic of high–redshift Ly_α emitters and the Ly_α forest continuum break.

Figure 13 shows a peculiar system of three sources: two emission-line sources above (~1.5 arcsecond) and below (~3 arcsecond) the main galaxy $GDS\ J033228.88-274129.3$, clearly visible in the ACS color image and in the two dimensional spectrum. The same target has been observed in two different masks adopting the same orientation of the slits. The total exposure time is ≃43 ks. The extracted one dimensional spectra are shown in the right side of the Figure 13.

The main galaxy $GDS\ J033228.88-274129.3$ has a redshift $z = 0.733$ with both emission and absorption lines measured (quality flag "A"): [O II]3727, MgI, Ca H and K, g-band, etc. The bottom object ($GDS\ J033228.84-274132.7$) shows a solo-emission line at 7052Å (see the 1-D spectrum), and is not detected in the ACS B band, we interpret this line as Ly_α at $z = 4.800$ with quality "C".

The source above $GDS\ J033228.88-274129.3$ is most probably a Ly_α emitter at redshift $z = 4.882$ (quality "B"). The spectrum has been extracted subtracting the contamination of the tail of the main galaxy. After the subtraction the shape of the spectrum shows the blue cut–off and the Ly_α forest continuum break, typical of the LBGs.

5.5. Dynamical masses of galaxies at $z \sim 1$

Three galaxies, $GDS\ J033215.88-274723.1$, $GDS\ J033225.86-275019.7$ and $GDS\ J033230.71-274617.2$, at redshift z=0.896, 1.095 and z=1.307 respectively show a spatially resolved [O II]3727 line with a characteristic "tilt" indicative of a high rotation velocity (see Figure 14).

Various studies have been carried out on the internal kinematics of distant galaxies (Vogt at al. 1996, Vogt at al. 1997, Moorwood et al. 2001, Pettini et al. 2001 and van Dokkum & Stanford 2001). Rigopoulou et al. 2002 have determined velocity profiles with a medium resolution grating R~5000 of three galaxies at z~0.6 and one at z~0.8, detected by ISOCAM in the HDF–S. For one object they have derived a rotational velocity of 460 km s^{-1} containing a mass of $10^{12} M_\odot$ (within a radius of 20 Kpc) significantly higher than the dynamical masses measured in most other local and high redshift spirals.

In the case of $GDS\ J033215.88-274723.1$, $GDS\ J033225.86-275019.7$ and $GDS\ J033230.71-274617.2$, the spectra, in spite of the relatively low resolution $\Re \sim 860$, clearly show a tilt of several pixels (corresponding to about 10Å). The measured velocity increases with increasing distance from the center of the objects reaching a value of the order of and greater than 400 km s^{-1} at the extremes. For the object $GDS\ J033225.86-275019.7$ we have measured a displacement between the two extreme peaks of 11.5Å (top panel of the Figure 14), while a displacement of 9.6Å has been measured in the case of $GDS\ J033215.88-274723.1$ (middle panel of the Figure 14)

Assuming that the observed velocity structure is due to dynamically-relaxed rotation, then it is possible to estimate the dynamical mass for the three galaxies shown in Figure 14 (e.g. Lequeux (1983)): $\frac{1.6}{sin^2(i)} \times 10^{11} M_\odot$ for the galaxy $GDS\ J033215.88-274723.1$ (within a radius of 7.8 Kpc) and $\frac{3.1}{sin^2(i)} \times 10^{11} M_\odot$ for the galaxy $GDS\ J033225.86-275019.7$ (within a radius of 9.8 Kpc). The noisy spectrum of the galaxy $GDS\ J033230.71-274617.2$ allows us to roughly measure a dynamical mass of the order of $\frac{1.5}{sin^2(i)} \times 10^{11} M_\odot$ (within a radius of 7.5 Kpc). The estimates should be considered a lower limit to the total dynamical mass because more external parts of the rotating structure might have a lower surface brightness and remain undetected.

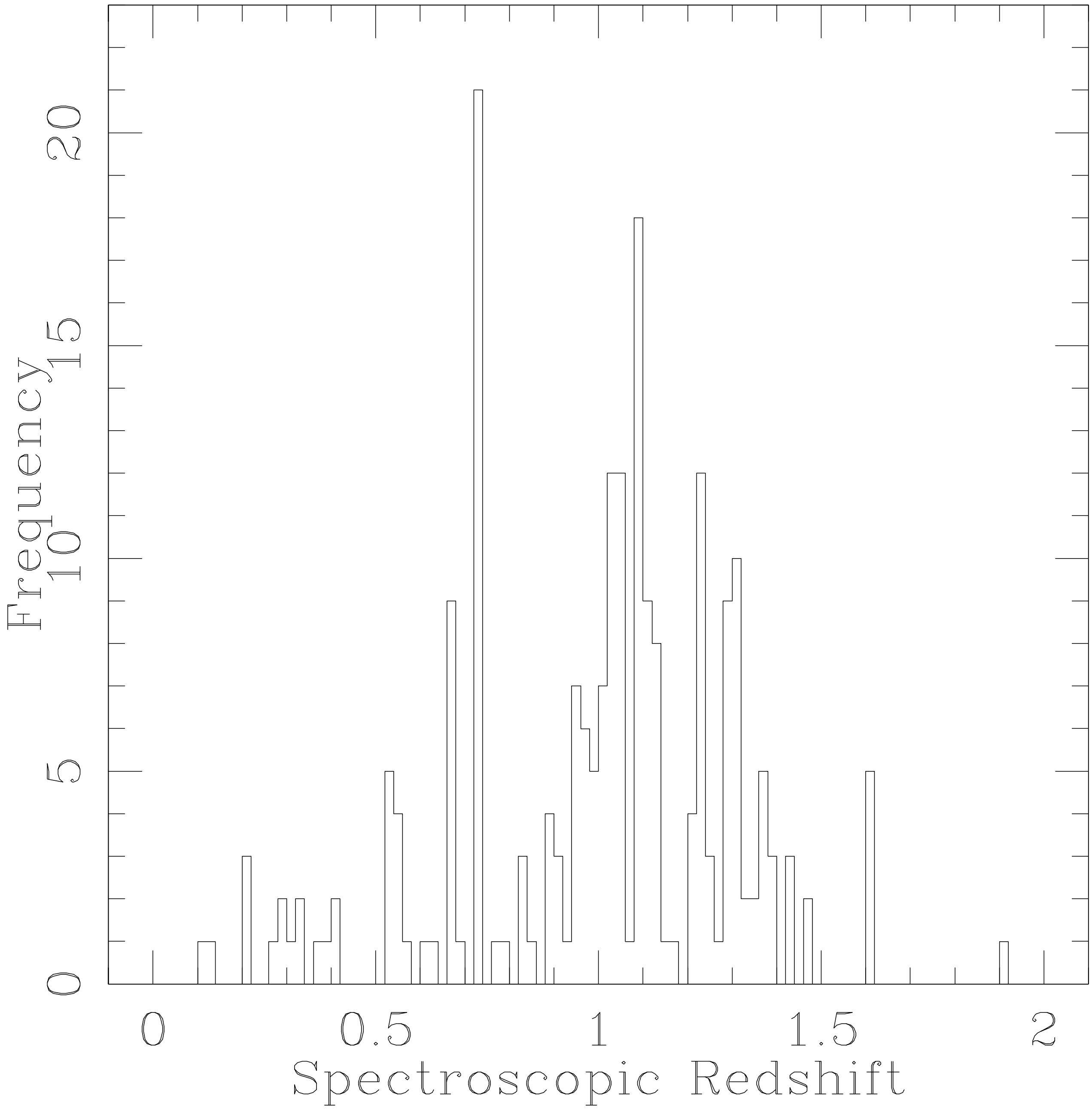

Fig. 9. Redshift distribution for the spectroscopic sample with quality A, B and C (23 redshift determinations out of 224 have quality C). Three objects at z>4 are not shown in the histogram.

5.6. GDS J033210.93 − 274721.5: a spectrum contaminated by a nearby galaxy.

The spectrum of the galaxy $GDS\ J033210.93-274721.5$ simultaneously shows features corresponding to the redshifts z=1.222 and z=0.417 (Figure 15). The origin of the overlap is the presence of a nearby galaxy ($z_{850}=19.98$, $GDS\ J033210.92-274722.8$) offset by 1.3 arcsecond with a redshift $z=0.417$. Light from the brighter $z=0.417$ galaxy contaminates the spectrum of the fainter ($z_{850}=22.19$), higher redshift galaxy $GDS\ J033210.93-274721.5$ (see Figure 15). Such cases may represent a problem and a source of error in large spectroscopic surveys, which require an highly automated data processing. A possible solution is to evaluate a priori on the basis of imaging what are the cases subject of light contamination requiring a “special” reduction. Alternatively, color-redshift diagrams (such as Figure 7), a comparison of spectroscopic and photometric redshifts or similar diagnostics are required to carry out the necessary data quality control and identify possible misidentifications.

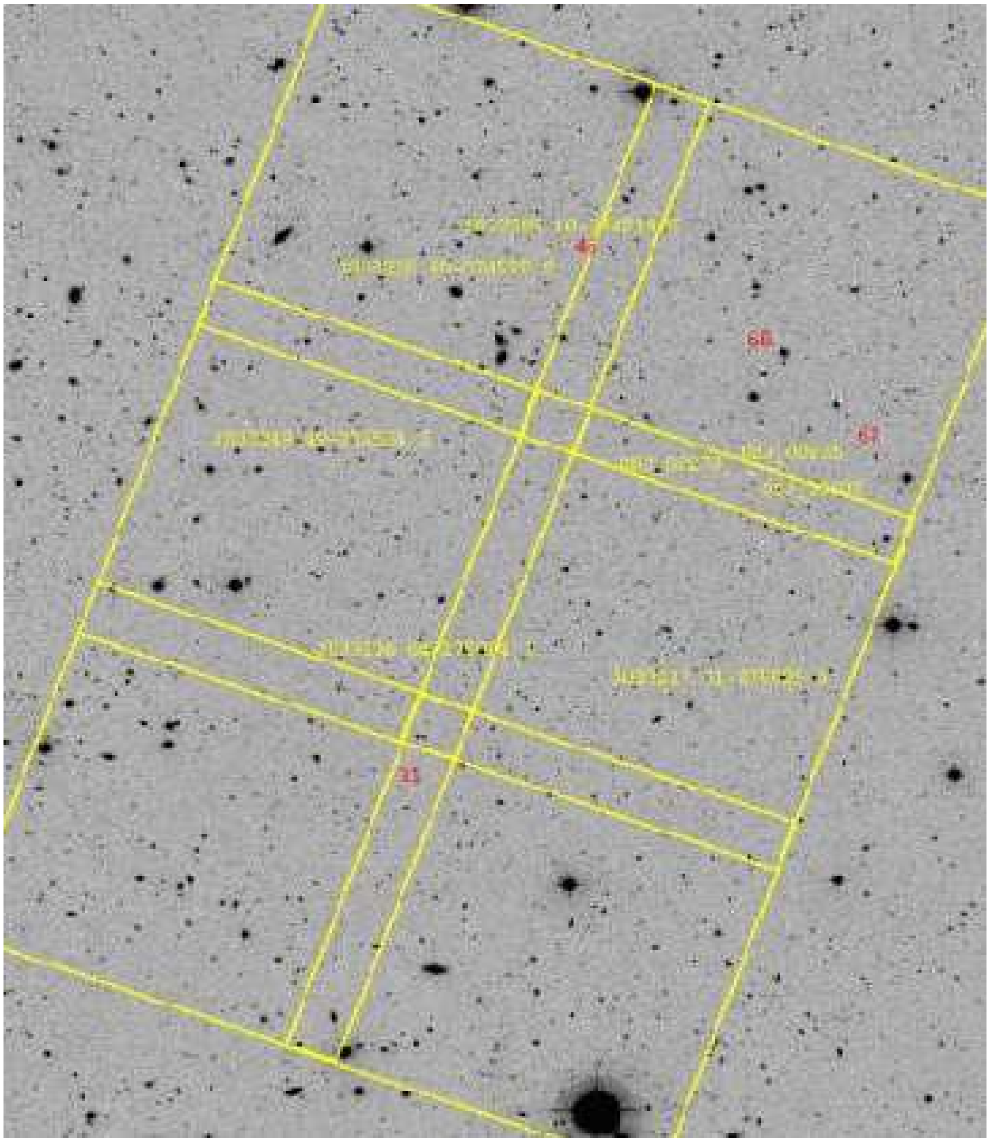

Fig. 10. The spatial distribution of the galaxies at $z \sim 1.61$ in the CDF-S. The background image is an exposure in the R band obtained with the ESO wide-field imager (WFI). North is up and east on the left. The squares represent the FOV of the FORS2 pointings. The five FORS2 targets are given by their coordinates, and the three K20 sources with the identifiers: OBJ_00235, OBJ_00237 and OBJ_00270. The numbers 31, 46, 60, 67, show the positions of $z \sim 1.61$ X-ray sources (see text).

6. Conclusions

In the framework of the Great Observatories Origins Deep Survey a large sample of galaxies in the Chandra Deep Field South has been spectroscopically targeted. A total of 303 objects with $z_{850} \lesssim 25.5$ has been observed with the FORS2 spectrograph at the ESO VLT providing 234 redshift determinations. From a variety of diagnostics the measurement of the redshifts appears to be highly accurate (with a typical $\sigma_z = 0.001$) and reliable (with an estimated rate of catastrophic misidentifications at most few percent). The reduced spectra and the derived redshifts are released to the community (*http://www.eso.org/science/goods/*). They constitute an essential contribution to reach the scientific goals of GOODS, providing the time coordinate needed to delineate the evolution of galaxy masses, morphologies, and star formation, calibrating the photometric redshifts that can be derived from the imaging data at 0.36-8μm and enabling detailed studies of the physical diagnostics for galaxies in the GOODS field.

Acknowledgements. We are grateful to the ESO staff in Paranal and Garching who greatly helped in the development of this programme. The work of DS was carried out at the Jet Propulsion Laboratory, California Institute of Technology, under a contract with NASA. L.A.M. acknowledges support by NASA through contract number 1224666 issued by the Jet Propulsion Laboratory, California Institute of Technology under NASA contract 1407. We thank the ASI grant I/R/088/02 (SC, MN, EV).

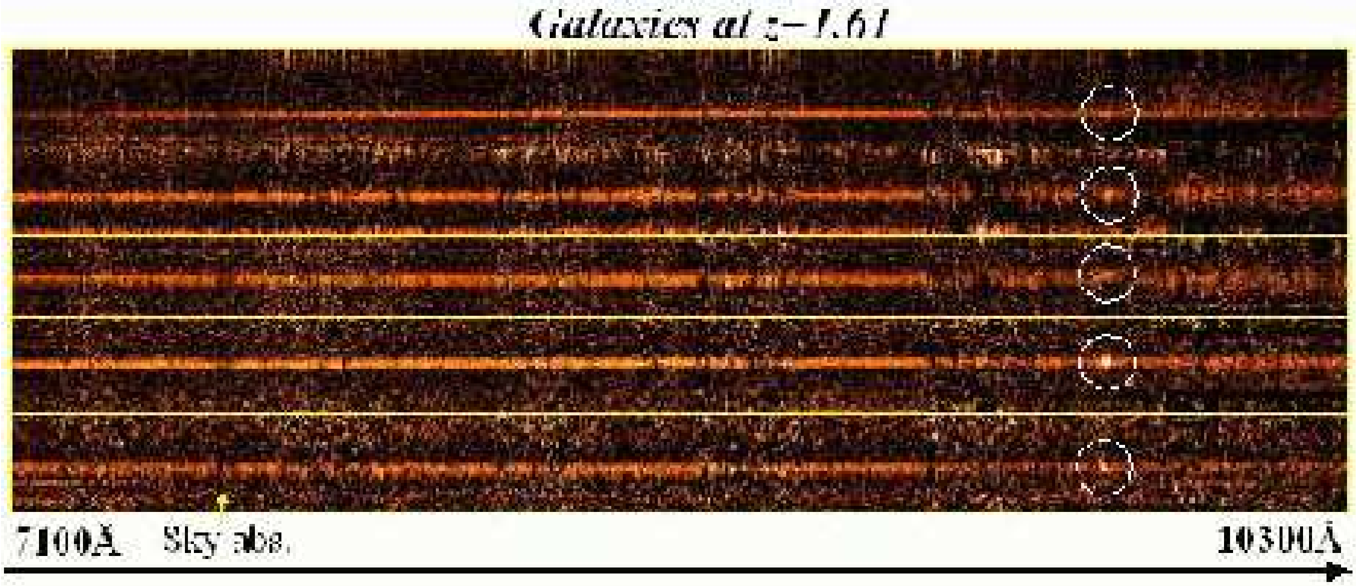

Fig. 11. Two dimensional spectra of 5 galaxies at z=1.61. The [O II]3727 emission line is marked with a circle at 9727.5Å. The absorption sky feature (~7600Å, A band) is indicated with an arrow. It is worth to note the optimal red sensitivity of FORS2.

References

Abraham, R., G., van den Bergh, S., Glazebrook, K., Ellis, R., S., Santiago, B., X., Surma, P., Griffiths, R., E., 1996, ApJ, 107, 1

Bahcall, J.N., Schmidt, M., Soneira, R.M. 1982, ApJ, 258, 17

Bohlin, R.,C., Colina, L., Finley, D., S., 1995, AJ, 110, 1316

Cimatti, A., Mignoli, M., Daddi, E., et al. 2002, A&A, 392, 395

Coleman, G., D., Wu, C.-C., & Weedman, D., W., 1980, ApJS, 43, 393

Dickinson et al. 2003, in the proceedings of the ESO/USM Workshop ”The Mass of Galaxies at Low and High Redshift” (Venice, Italy, October 2001), eds. R. Bender and A. Renzini, astro-ph/0204213

Dickinson, M., et al., 2004, ApJ, 99, 122

Giavalisco, M., et al. 2004, ApJ, 600, L93

Giavalisco, M., Dickinson, M., Ferguson, H. C., Ravindranath, S., Kretchmer, C., Moustakas, L. A., Madau, P., Fall, S. M., Gardner, Jonathan P., Livio, M., Papovich, C., Renzini, A., Spinrad, H., Stern, D., Riess, A., 2004, ApJ, 600, 103

Gilli, R., Cimatti, A., Daddi, E., Hasinger, G., Rosati, P., Szokoly, G., Tozzi, P., Bergeron, J., Borgani, S., Giacconi, R., Kewley, L., Mainieri, V., Mignoli, M., Nonino, M., Norman, C., Wang, J., Zamorani, G., Zheng, W., Zirm, A., 2003, ApJ, 592, 721

Le Fevre, O., Vettolani, G., Paltani, S., Tresse, L., Zamorani, G., Le Brun, V., Moreau, C., and the VIMOS VLT Deep Survey team, submitted to A&A, (astro-ph/0403628)

Lequeux, J. 1983, A&A, 125, 394

Moorwood A.F.M., van der Werf, P.P, Cuby, J.G., Oliva, E., 2000, A&A, 362, 9

Mobasher, B., Idzi, R., Bentez, N., Cimatti, A., Cristiani, S., Daddi, E., Dahlen, T., Dickinson, M., et al., 2004, ApJ, 600, 167

Oke, J.B., et al., 1995, PASP, 107, 375

Pettini, M., Shapley, A. E., Steidel C. C., Cuby, J.-G., Dickinson, M., A. F. M. Moorwood, Adelberger, K. L., Giavalisco, M., 2001, ApJ, 588, 65

Renzini et al. 2002, in the proceedings of the ESO/USM Workshop ”The Mass of Galaxies at Low and High Redshift” (Venice, Italy, October 2001), eds. R. Bender and A. Renzini

Riess, A.G.,2 Strolger, L.-G., Tonry, J., Casertano, S., Ferguson, H.C., et al., 2004, ApJ, 607, 665

Rigopoulou, D., Franceschini, A., Aussel, H., Genzel, R., Thatte, N., Cesarsky, C. J., 2002, ApJ, 580, 789

Steidel, C.C., Adelberger, K.L., Giavalisco, M., Dickinson, M., Pettini, M., 1999, ApJ, 519, 1

Szokoly, G., P., Bergeron, J., Hasinger, G., Lehmann, I., Kewley, L., Mainieri, V., Nonino, M., Rosati, P., Giacconi, R., Gilli, R., Gilmozzi, R., Norman, C., Romaniello, M., Schreier, E., Tozzi, P., Wang, J., X., Zheng, W., Zirm, A., 2004, (astro-ph/0312324)

van Dokkum, P.G., & Stanford, S.A. 2001, ApJ, 562, 35

Vogt, P.N., et al. 1996, ApJ, 465, L15

Vogt, P.N., et al. 1996, ApJ, 479, L121

Warmels, R.H.: 1991, “The ESO-MIDAS System”, in Astronomical Data Analysis Software and Systems I , PASP Conf. Series, Vol. 25, p. 115.

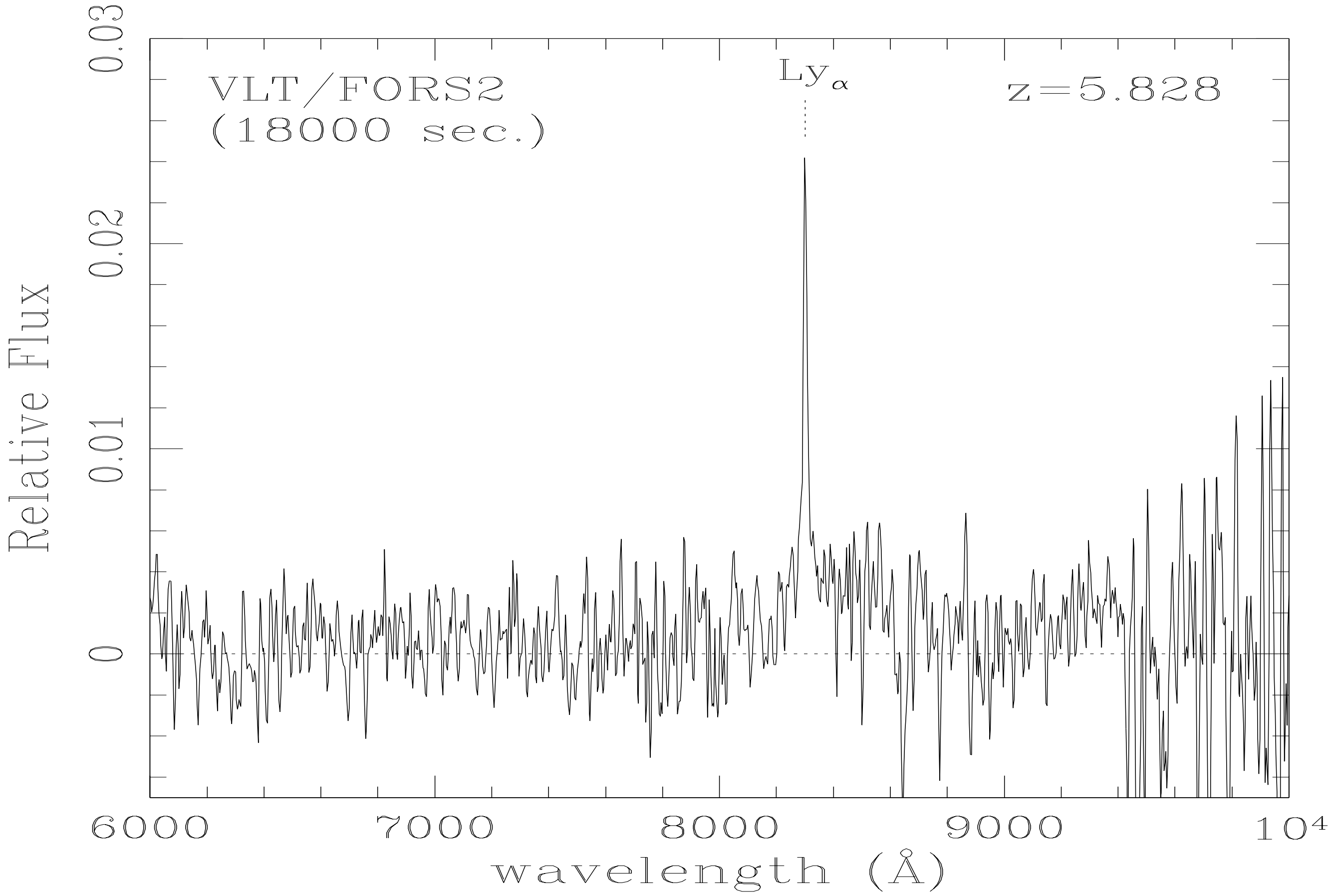

Fig. 12. VLT spectrum of the i_{775}–dropout galaxy GDS J033240.01-274815.0.

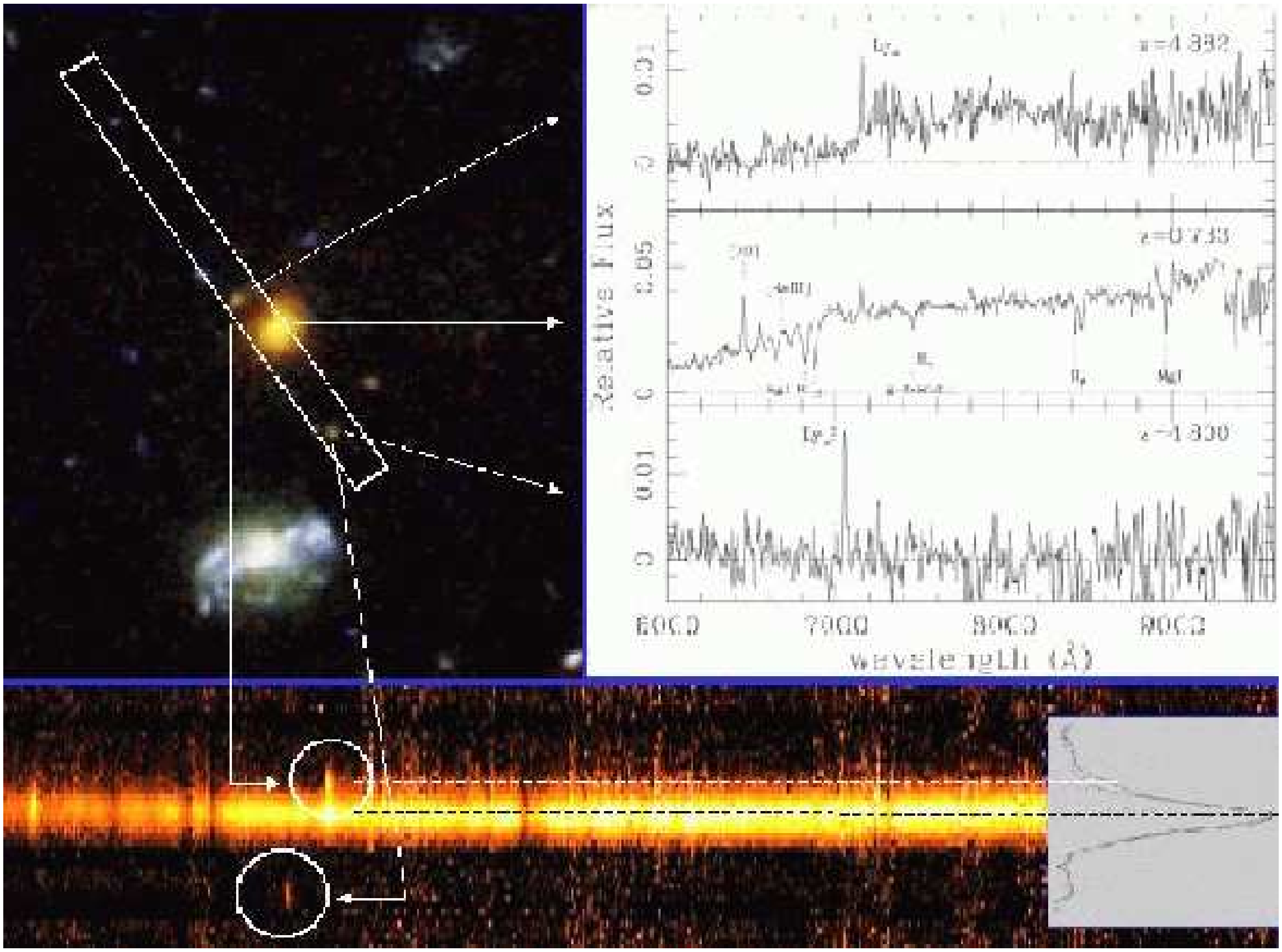

Fig. 13. Simultaneous spectrum of three sources in the slit. On the right of the figure, the 1D spectra of the z=0.733 main galaxy *GDS J*033228.88 – 274129.3, the single emission line ∼ 3 arcsecond below (*GDS J*033228.84 – 274132.7) and the object ∼ 1.5 arcsecond above are shown. The left-hand panel shows the ACS color image, 5 arcsec on a side. North is up, east is to the left. The bottom panel shows the 2D spectrum, with the spatial profile obtained by collapsing 80 columns (256 Å), centered at 7150Å, shown to the right. Candidate serendipitous Ly_α emission lines are clearly marked. The object above the target source shows faint continuum reward of the emission line.

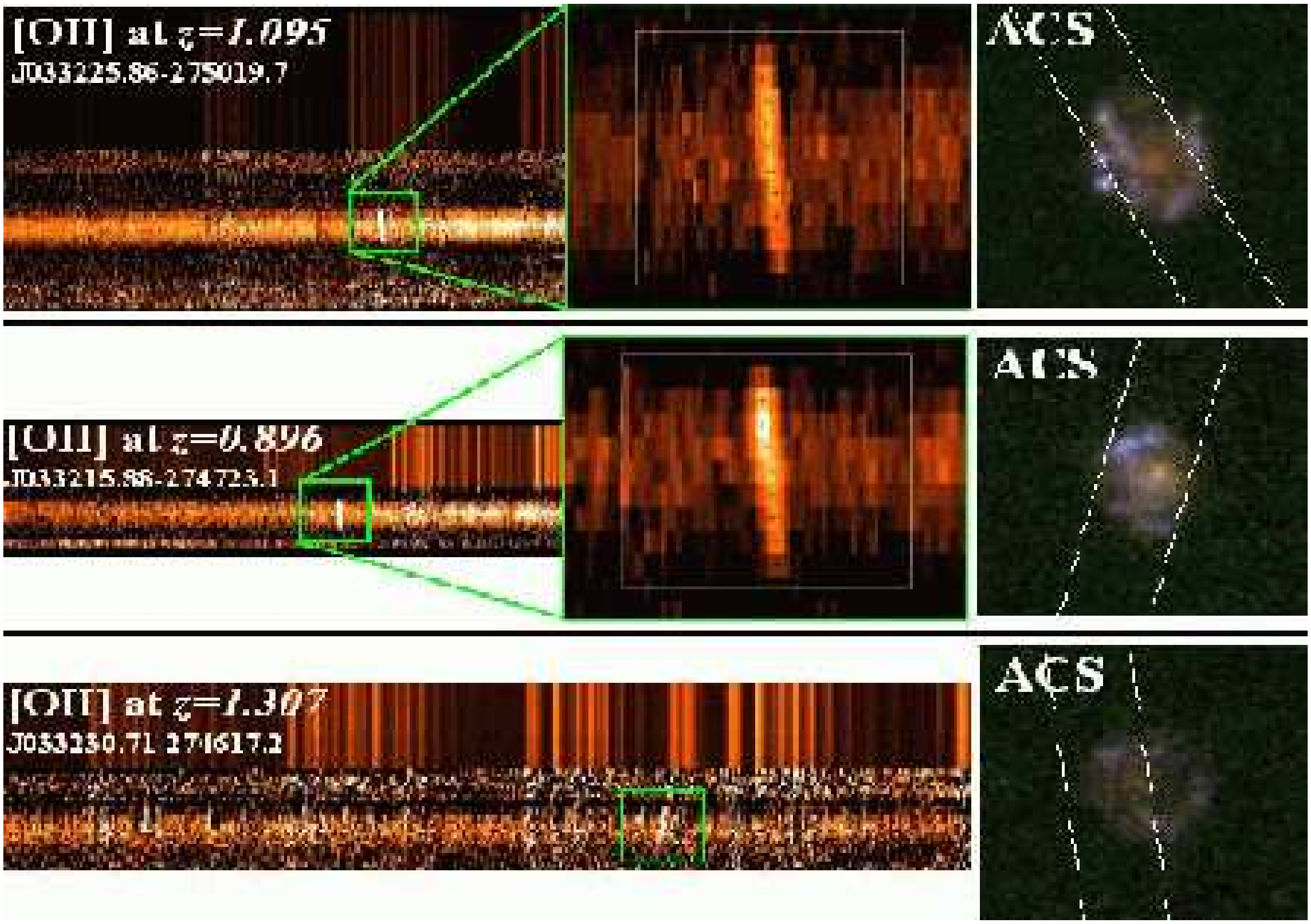

Fig. 14. Three examples of tilted [O ɪɪ]3727 emission line at redshift around 1. The two dimensional FORS2 spectra are shown (object and sky lines). In the first two spectra (top and middle) a zoom of the [O ɪɪ]3727 emission line is shown (the white rectangle underline the region where the Gaussian fit has been performed to derive the line peak, small black crosses), in the bottom spectrum the line is too faint to calculate a reliable peak (this object has been serendipitously-identified). In the right side of the spectra the ACS images of the galaxies and the slits orientation are shown.

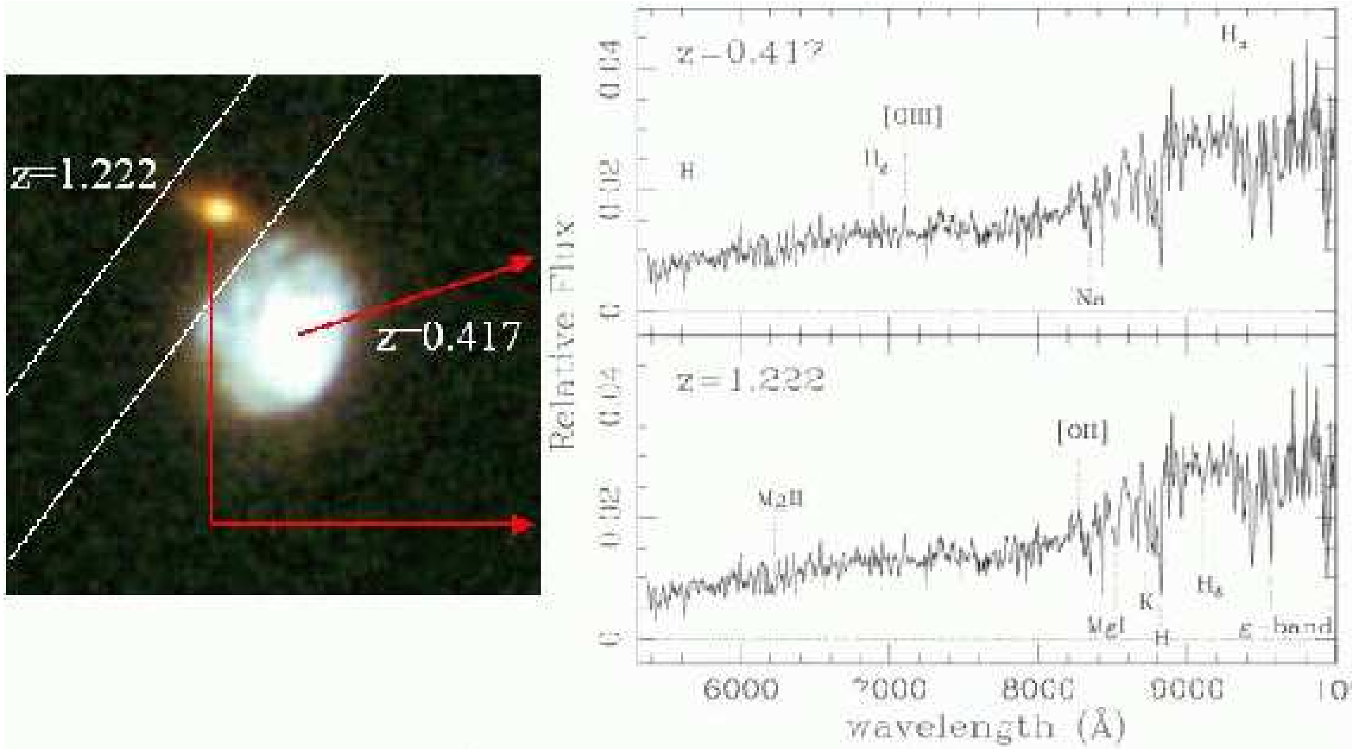

Fig. 15. The light merged case, two objects at different redshift superimposed in the slit (marked with white lines in the left panel). In the right panel the same extracted spectrum with different identifications. An elliptical galaxy (the target, *GDS J*033210.93 – 274721.5) at z=1.222 clearly identified with the Ca H and K, Hδ, MgI (quality flag “A”). The bright bluer object (*GDS J*033210.92 – 274722.8) shows absorption and emission lines: Ca H, [O III]5007, Na, Hα at $z = 0.417$ (quality flag “B”). The Ca K is contaminated by the sky line ~5577Å.